Article

Cell Reports

# Failed Progenitor Specification Underlies the Cardiopharyngeal Phenotypes in a Zebrafish Model of 22q11.2 Deletion Syndrome

## Graphical Abstract

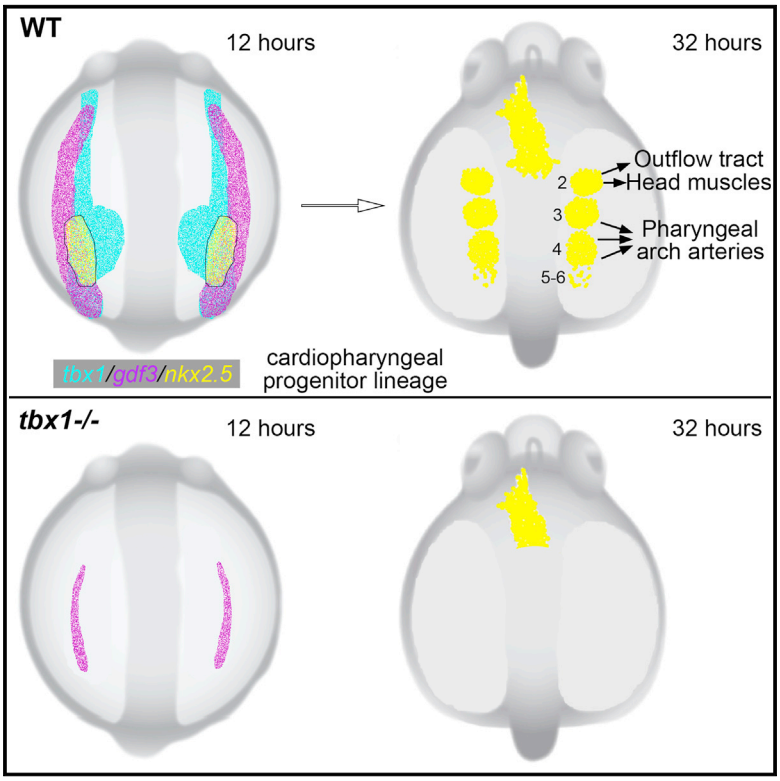


## Highlights

- Zebrafish *tbx1* mutants display defects analogous to those in *22q11.2DS* patients
- Mutants fail to specify *nkx2.5*$^{+}$ progenitors that generate the affected structures
- Intersectional expression of *tbx1*, *gdf3*, and *nkx2.5* defines these progenitors
- The Gdf3 receptor ALK4 acts downstream of *tbx1* in progenitor specification

## Authors

Burcu Guner-Ataman, Juan Manuel González-Rosa, Harsh N. Shah, ..., Laurie A. Boyer, C. Geoffrey Burns, Caroline E. Burns

## Correspondence

gburns@cvrc.mgh.harvard.edu (C.G.B.), cburns6@mgh.harvard.edu (C.E.B.)

## In Brief

Microdeletions encompassing the *TBX1* locus cause 22q11.2 deletion syndrome (DS), which is characterized by congenital heart, aorta, and craniofacial malformations. Using a zebrafish model of 22q11.2DS, Guner-Ataman et al. demonstrate that *tbx1*-mutant animals fail to specify the *nkx2.5*$^{+}$ progenitor population that gives rise to the affected structures.

Guner-Ataman et al., 2018, Cell Reports *24*, 1342–1354
July 31, 2018 
https://doi.org/10.1016/j.celrep.2018.06.117

CellPress

OPEN ACCESS
CellPress

Cell Reports
Article

# Failed Progenitor Specification Underlies the Cardiopharyngeal Phenotypes in a Zebrafish Model of 22q11.2 Deletion Syndrome

Burcu Guner-Ataman,[1,2] Juan Manuel González-Rosa,[1,2] Harsh N. Shah,[1] Vincent L. Butty,[3] Spencer Jeffrey,[1] Maryline Abrial,[1,2] Laurie A. Boyer,[3] C. Geoffrey Burns,[1,2,*] and Caroline E. Burns[1,2,4,5,*]
[1]Cardiovascular Research Center, Massachusetts General Hospital, Charlestown, MA 02129, USA
[2]Harvard Medical School, Boston, MA 02115, USA
[3]Department of Biology, Massachusetts Institute of Technology, 77 Massachusetts Avenue, Cambridge, MA 02139, USA
[4]Harvard Stem Cell Institute, Cambridge, MA 02138, USA
[5]Lead Contact
*Correspondence: gburns@cvrc.mgh.harvard.edu (C.G.B.), cburns6@mgh.harvard.edu (C.E.B.)
https://doi.org/10.1016/j.celrep.2018.06.117

## SUMMARY

**Microdeletions involving TBX1 result in variable congenital malformations known collectively as 22q11.2 deletion syndrome (22q11.2DS). Tbx1-deficient mice and zebrafish recapitulate several disease phenotypes, including pharyngeal arch artery (PAA), head muscle (HM), and cardiac outflow tract (OFT) deficiencies. In zebrafish, these structures arise from *nkx2.5*$^+$ progenitors in pharyngeal arches 2–6. Because pharyngeal arch morphogenesis is compromised in Tbx1-deficient animals, the malformations were considered secondary. Here, we report that the PAA, HM, and OFT phenotypes in *tbx1* mutant zebrafish are primary and arise prior to pharyngeal arch morphogenesis from failed specification of the *nkx2.5*$^+$ pharyngeal lineage. Through *in situ* analysis and lineage tracing, we reveal that *nkx2.5* and *tbx1* are co-expressed in this progenitor population. Furthermore, we present evidence suggesting that *gdf3*-ALK4 signaling is a downstream mediator of *nkx2.5*$^+$ pharyngeal lineage specification. Collectively, these studies support a cellular mechanism potentially underlying the cardiovascular and craniofacial defects observed in the 22q11.2DS population.**

## INTRODUCTION

22q11.2 deletion syndrome (22q11.2DS) is the most common deletion syndrome in humans, affecting ~1 in 4,000 live births and an unknown number of fetuses that die *in utero* (Botto et al., 2003; McDonald-McGinn et al., 1997, 2015; Ryan et al., 1997; Scambler, 2000, 2010). The clinical features associated with 22q11.2DS have been attributed to haploinsufficiency of *TBX1*, a gene in the typically deleted region (Lewin et al., 1997; Rauch et al., 1998; Ryan et al., 1997; Yagi et al., 2003). Among a broad spectrum of potential abnormalities that include cardiovascular deficiencies, abnormal facial development, cleft palate, and endocrine gland hypoplasia, those affecting the cardiac outflow tract and aortic arch are the main causes of mortality during childhood (McDonald-McGinn et al., 2015; Scambler, 2000). Interestingly, ~25% of individuals harboring the deletion show no discernable cardiovascular pathology, underscoring the complexity and variable nature of the disease (McDonald-McGinn et al., 2015). This confounding observation suggests that genetic, epigenetic, and/or environmental modifiers determine disease severity in the 22q11.2DS population (McDonald-McGinn et al., 2015).

Many of the tissues affected in 22q11.2DS patients are malformed or absent in *Tbx1*-deficient mice (Jerome and Papaioannou, 2001; Kelly et al., 2004; Lindsay and Baldini, 2001; Merscher et al., 2001; Vitelli et al., 2002) and zebrafish (Hami et al., 2011; Nevis et al., 2013; Piotrowski et al., 2003; Piotrowski and Nüsslein-Volhard, 2000) including the pharyngeal arch arteries (PAAs), head muscles (HMs), and cardiac outflow tract (OFT). Interestingly, all of these structures derive from the pharyngeal apparatus, a transient series of grooves, arches, and pouches that form by segmentation on the lateral surface of the embryonic head (Graham, 2003). Because morphogenetic pharyngeal segmentation is severely compromised in *Tbx1*-deficient animals (Jerome and Papaioannou, 2001; Piotrowski and Nüsslein-Volhard, 2000; Vitelli et al., 2002), their congenital malformations have traditionally been considered secondary (Arnold et al., 2006; Jerome and Papaioannou, 2001; Kelly et al., 2004; Kochilas et al., 2002; Liao et al., 2004; McDonald-McGinn et al., 2015; Merscher et al., 2001).

Recently, we reported that the PAAs, pharyngeal arch (PA) 2-derived HMs, and cardiac OFT in zebrafish descend from *nkx2.5*$^+$ progenitor cells that are specified in anterior lateral plate mesoderm (ALPM) before becoming sequestered in the cores of PAs 2–6 (Paffett-Lugassy et al., 2017). Those progenitors housed in PA2 give rise to five HMs and three OFT lineages (endothelium, myocardium, and smooth muscle) (Paffett-Lugassy et al., 2017), whereas those in PAs 3–6 give rise to the endothelial linings of their respective PAA (Paffett-Lugassy et al., 2013). Here, we report the unexpected observation that these progenitors, termed the *nkx2.5*$^+$ pharyngeal lineage, fail to be specified in *tbx1* mutant zebrafish embryos. Importantly, this defect

precedes the timing of pharyngeal arch morphogenesis, which rules out abnormal segmentation as a root cause. In addition, we identify *gdf3* (previously known as *vg1* or *dvr1*), the single zebrafish homolog of mammalian *GDF1* and *GDF3* (Bisgrove et al., 2017; Montague and Schier, 2017; Pelliccia et al., 2017), as downstream of Tbx1 and its receptor ALK4 as a mediator of *nkx2.5*$^+$ pharyngeal progenitor specification. Taken together, our studies highlight a paradigm to potentially explain the cardiovascular and craniofacial defects observed in the 22q11.2DS population.

## RESULTS

### Tbx1 Is Required for Pharyngeal Arch Artery, HM, and OFT Morphogenesis in Zebrafish

Previous studies have demonstrated that *tbx1* mutant zebrafish embryos, originally termed *van gogh* (*vgo*) (Piotrowski et al., 2003, 1996; Piotrowski and Nüsslein-Volhard, 2000), lack blood flow through PAAs 3–6 based on failed perfusion by ink (Piotrowski and Nüsslein-Volhard, 2000) or fluorescent microbeads (Piotrowski et al., 2003). To learn whether this phenotype reflects an absence of PAA endothelium, rather than a lack of patency, we examined PAs 3–6 in 72 hr post-fertilization (hpf) control animals and *tbx1* mutants carrying the transgenic endothelial reporter *kdrl:GFP* (Choi et al., 2007). Whereas control animals displayed robust GFP fluorescence in the endothelia of PAAs 3–6 (Figures 1A and 1B), *tbx1* mutants were devoid of these vessels (Figures 1C and 1D), which is a phenotype shared with *Tbx1* null mice (Lindsay and Baldini, 2001; Xu et al., 2005; Zhang et al., 2006). Previous studies in zebrafish have revealed that the PAAs arise by vasculogenesis from clusters of *tie1*$^+$ angioblasts that differentiate from *nkx2.5*$^+$ pharyngeal progenitors embedded in the PAs (Abrial et al., 2017; Anderson et al., 2008; Paffett-Lugassy et al., 2013). Therefore, we evaluated *tbx1* mutants for the presence or absence of PAA angioblast clusters at 38 hpf. In contrast to control animals, which displayed prominent clusters in PAs 3–5 (Figures 1E and 1F), *tbx1* mutants were devoid of this angioblast population (Figures 1G and 1H). These data demonstrate that Tbx1 is crucial for PAA endothelial establishment in zebrafish.

HM defects were also noted in the original characterization of *tbx1* mutants (Piotrowski and Nüsslein-Volhard, 2000). To characterize this phenotype at higher resolution, we analyzed *tbx1* mutants immunostained with the striated muscle-specific antibody MF20. From this analysis, we learned that *tbx1* mutants display underdeveloped and/or mispatterned dorsal, middle, and ventral HMs derived from PA1 and PA2 (Schilling and Kimmel, 1997) (Figures 1I–1L). These HM phenotypes are reminiscent of those in *Tbx1* null mice (Kelly et al., 2004; Kong et al., 2014) and implicate Tbx1 in the formation of PA1- and PA2-derived HMs in zebrafish. In addition to PAA endothelial and HM phenotypes, *tbx1* mutant animals also exhibit previously described OFT deficiencies (Hami et al., 2011; Nevis et al., 2013) (Figures 1I and 1K), which are similar to those observed in *Tbx1* null mice (Lindsay et al., 1999; Xu et al., 2004; Zhang et al., 2006). Together, these data demonstrate that the constellation of cardiopharyngeal phenotypes in Tbx1-deficient zebrafish and mice, particularly those affecting the PAAs, HMs, and OFT, is highly overlapping and reminiscent of 22q11.2DS.

### *tbx1* Mutant Zebrafish Embryos Lack *nkx2.5*$^+$ Pharyngeal Progenitors

We were intrigued by this collection of phenotypes given our recent observation that all of the affected structures, except the PA1-derived HMs, descend from the pharyngeal subset of *nkx2.5*$^+$ progenitor cells specified in the ALPM (Paffett-Lugassy et al., 2017). This subset becomes sequestered into the mesodermal cores of PAs 2–6 before differentiating into mature structures. The progenitors in PA2 give rise to HM and OFT lineages (Paffett-Lugassy et al., 2017), whereas those in PAs 3–6 give rise to PAA endothelium (Paffett-Lugassy et al., 2013). The other subset of *nkx2.5*$^+$ progenitors specified in the ALPM produces ventricular myocardium (Guner-Ataman et al., 2013; Paffett-Lugassy et al., 2017; Schoenebeck et al., 2007; Serbedzija et al., 1998).

To directly evaluate the *nkx2.5*$^+$ pharyngeal progenitor subpopulation in *tbx1* mutants, we analyzed control and mutant embryos carrying the *nkx2.5:ZsYellow* transgene (Zhou et al., 2011). At 32 hpf, control animals displayed ZsYellow$^+$ fluorescence in the heart tube and pharyngeal clusters embedded in PAs 2–4 (Paffett-Lugassy et al., 2013) (Figure 2A). In *tbx1* mutants, whereas ZsYellow was observed in the heart, the pharyngeal clusters were absent (Figure 2B), which explains the loss of their derivatives at later stages (Figures 1A–1L). Using *in situ* hybridization, we confirmed that endogenous *nkx2.5* transcripts were also absent in the pharyngeal arches (Figures 2C and 2D). This phenotype resembles that of *Tbx1* null mice, which exhibit reduced expression of cardiopharyngeal progenitor markers in analogous regions at embryonic day (E) 8.5 and E9.5 (Kelly and Papaioannou, 2007).

Previous studies have revealed that *tbx1* mutants exhibit profound deficiencies in pharyngeal segmentation, specifically at the level of endodermal pouch formation (Arnold et al., 2006; Choe and Crump, 2014; Merscher et al., 2001; Piotrowski and Nüsslein-Volhard, 2000). Therefore, the observed absence of *nkx2.5*$^+$ pharyngeal clusters in 32 hpf *tbx1* mutants (Figures 2A–2D) could be a secondary consequence of faulty pharyngeal segmentation. To test this hypothesis, we evaluated mutant animals for ZsYellow fluorescence earlier in development (20 hpf) when only pouches 1 and 2 of 6 total have formed (Choe and Crump, 2014; Schilling and Kimmel, 1994). At this stage, *tbx1* embryos also lacked *nkx2.5:ZsYellow*$^+$ (Figures 2E and 2F) and *nkx2.5*$^+$ (Figures 2G and 2H) pharyngeal clusters, demonstrating that the absence of *nkx2.5*$^+$ pharyngeal progenitors in *tbx1* mutants is already evident early in the segmentation window and is therefore unlikely to be secondary.

### Tbx1 Is Required for Specification of the *nkx2.5*$^+$ Pharyngeal Progenitor Lineage in the ALPM of Zebrafish Embryos

Endogenous *nkx2.5* transcripts have been documented by *in situ* hybridization in the zebrafish ALPM as early as 6 somite stage (ss; 12 hpf) (Lee et al., 1996; Schoenebeck et al., 2007), a time that precedes pharyngeal segmentation (Schilling and Kimmel, 1994). We refined the timing of *nkx2.5* transcriptional onset by

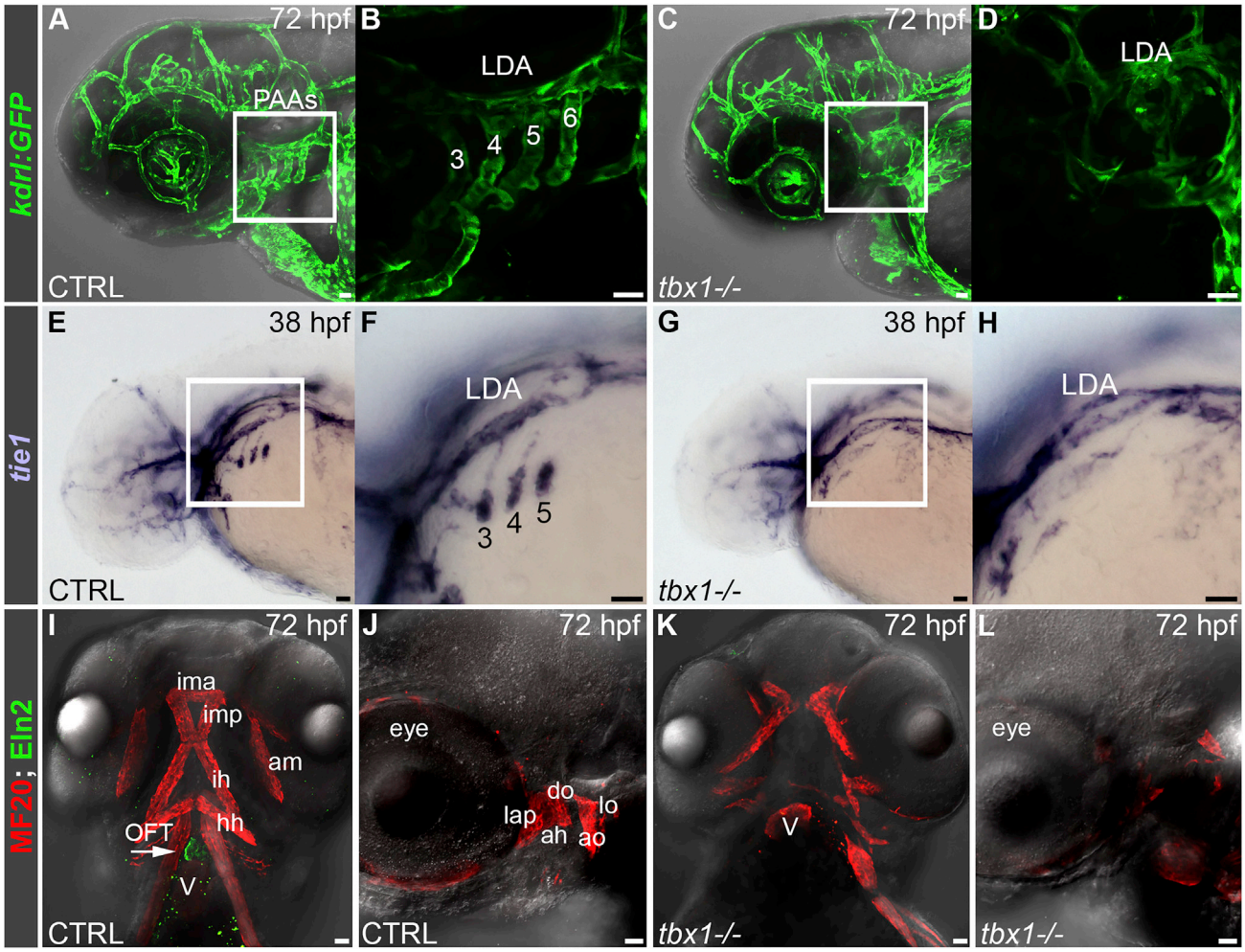


**Figure 1. Tbx1 Is Required for Pharyngeal Arch Artery, Head Muscle, and Outflow Tract Morphogenesis in Zebrafish**

(A–D) Confocal z-stacks of the head (A and C) and pharyngeal arch arteries (PAAs; B and D) in live 72 hr post-fertilization (hpf) control (CTRL; A and B; n = 60) and *tbx1* mutant (C and D; n = 20) embryos carrying the *Tg(kdrl:GFP)* endothelial reporter. (B) and (D) are independent z-stacks acquired at higher magnification of the boxed regions in (A) and (C). Merged bright-field images and confocal z-stacks are shown in (A) and (C). The numbers in (B) identify each PAA. Lateral views, anterior left.

(E–H) Bright-field z-stacks of the head (E and G) and pharyngeal arches (F and H) in 38 hpf CTRL (E and F; n = 40) and *tbx1* mutant (G and H; n = 19) embryos processed by *in situ* hybridization with a *tie1* riboprobe. The boxed regions in (E) and (G) are shown at higher magnification in (F) and (H). The numbers in (F) identify each *tie1*$^{+}$ PAA angioblast cluster. Lateral views, anterior left.

(I–L) Merged bright-field images and confocal z-stacks of the head region in 72 hpf CTRL (I and J; n = 40) and *tbx1* mutant (K and L; n = 19) embryos co-immunostained with antibodies recognizing striated muscle (MF20, red) or OFT smooth muscle (Eln2, green). Ventral views, anterior up in (I) and (K). Lateral views, anterior left in (J) and (L). Arrow in (I) highlights the Eln2$^{+}$ OFT smooth muscle that is missing in *tbx1* mutants. In all cases, little to no variation was observed between animals in each experimental group.

Scale bars, 25 μm. Pharyngeal arch1 (PA1)-derived head muscles: am, abductor mandibulae; do, dilator operculi; ima, intermandibularis anterior; imp, intermandibularis posterior; lap, levator arcus palatini; PA2-derived head muscles: ah, adductor hyoideus; ao, adductor operculi; hh, hyohyoidus; ih, interhyoidus; lo, levator operculi. LDA, lateral dorsal aorta; OFT, outflow tract; PAAs, pharyngeal arch arteries; V, ventricle.

analyzing embryos at two earlier stages, tail bud (10 hpf) and 2 ss (~10.75 hpf), which bookmark the beginning of somitogenesis. Although no expression was observed at the tail bud stage, a bilateral domain of *nkx2.5* expression initiated at 2 ss (Figure 3A), indicating that *nkx2.5* expression commences concurrently with somite emergence. At 6, 10, and 14 ss (Figures 3B–3D), the domain grows in size prior to segregating into midline ventricular myocardial and lateral pharyngeal populations (Paffett-Lugassy et al., 2013, 2017). In contrast to control animals, *nkx2.5* expression was not detectable at 2 or 6 ss in *tbx1* mutants (Figures 3E and 3F). However, the bilateral *nkx2.5*$^{+}$ domain became visible by the 10 ss (Figure 3G), but was comparatively smaller, both in width and length, than that in control embryos at the same stage (Figure 3C). At the 14 ss, the *nkx2.5* expression domain remained smaller in the mutant (Figures 3D and 3H). Interestingly, *hand2* expression, which spans the width of the ALPM and

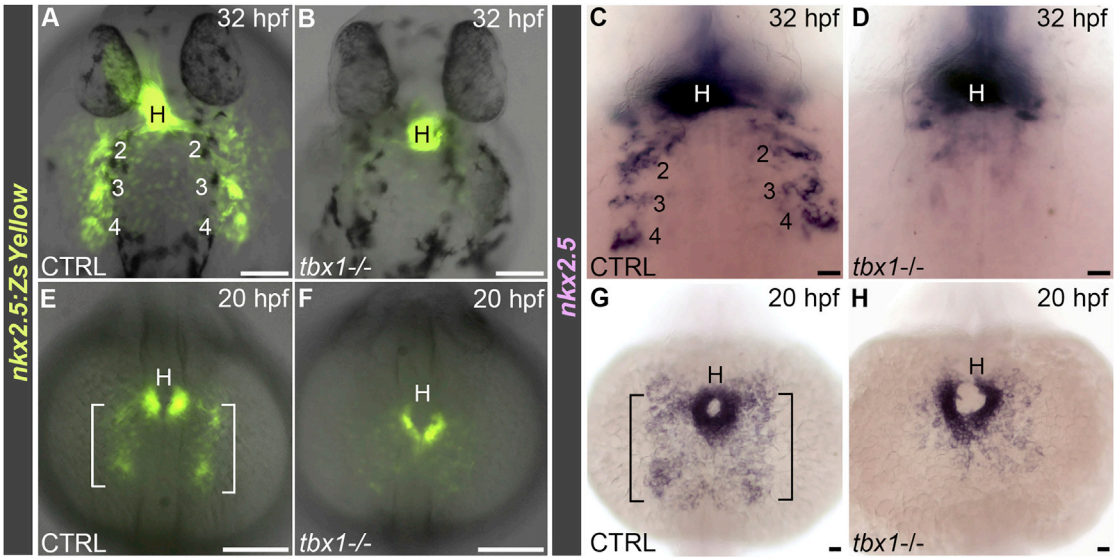


**Figure 2. *tbx1* Mutant Embryos Lack *nkx2.5*$^{+}$ Pharyngeal Progenitors**

(A and B) Merged bright-field and fluorescent images of 32 hr post fertilization (hpf) control (CTRL; A; n = 30) and *tbx1* mutant (B; n = 8) embryos carrying the *Tg(nkx2.5:ZsYellow)* transgene. Dorsal views, anterior up. The numbers in (A) identify each pharyngeal cluster.

(C and D) Bright-field z-stacks of 32 hpf CTRL (C; n = 51) and *tbx1* mutant (D; n = 18) embryos processed by *in situ* hybridization with an *nkx2.5* riboprobe. The numbers in (C) identify each pharyngeal cluster. Dorsal views, anterior up.

(E and F) Merged bright-field and fluorescent images of 20 hpf CTRL (E; n = 30) and *tbx1* mutant (F; n = 8) embryos carrying the *Tg(nkx2.5:ZsYellow)* transgene. The brackets in (E) highlight the ZsYellow$^{+}$ the pharyngeal progenitor population missing in (F). Dorsal views, anterior up.

(G and H) Bright-field z-stacks of 20 hpf CTRL (G; n = 32) and *tbx1* mutant (H; n = 10) embryos processed by *in situ* hybridization with an *nkx2.5* riboprobe. The brackets in (G) highlight the *nkx2.5*$^{+}$ pharyngeal progenitor population missing in (H). Dorsal views, anterior up. In all cases, little to no variation was observed between animals in each experimental group.

Scale bars, 25 μm. H, heart.

overlaps the medial *nkx2.5*$^{+}$ domain (Schoenebeck et al., 2007), was unaffected in *tbx1* mutants (Figures 3I and 3J), suggesting that the ALPM is not reduced in size but fails instead to adopt an *nkx2.5*$^{+}$ identity at 6 ss. Taken together, these data uncover a delay in the initiation of *nkx2*.5 ALPM expression and a reduced *nkx2.5*$^{+}$ field size at all stages analyzed in *tbx1* mutants. Importantly, we stage-matched control and mutant animals based on somite number, which eliminates the possibility that the observed phenotype resulted from generalized developmental delay. Lastly, we ruled out increased rates of apoptosis as the cause of delayed and reduced *nkx2.5* expression in the ALPM of mutant animals (Figures S1A–S1D).

A previous study from our laboratory demonstrated that *nkx2.5*$^{+}$ ventricular myocardial progenitors are specified normally in *tbx1* mutant animals (Nevis et al., 2013). This information, coupled with the observation that *nkx2.5*$^{+}$ pharyngeal progenitors are absent at 20 hpf (Figures 2E–2H), suggests that the lack of *nkx2.5* expression at 2 ss to 6 ss (Figures 3A, 3B, 3E, and 3F) and subsequent reductions in field size at 10 ss and 14 ss (Figures 3C, 3D, 3G, and 3H) result from failed specification of the pharyngeal lineage within the *nkx2.5*$^{+}$ domain. In other words, the *nkx2.5*$^{+}$ transcripts that remain in *tbx1* mutants are likely to be marking the ventricular myocardial lineage exclusively. To test this hypothesis, we prospectively lineage traced *nkx2.5*$^{+}$ progenitors in *tbx1* mutant animals using a previously validated transgenic strain, *Tg(nkx2.5:Kaede)*, which expresses the photoconvertible Kaede protein from *nkx2.5 cis*-regulatory elements (Guner-Ataman et al., 2013; Paffett-Lugassy et al., 2013). We pan-photoconverted Kaede$^{+}$ cells in control and *tbx1* mutants at 16 ss, when fluorescence is first detectable, and analyzed embryos for the localization of photoconverted Kaede protein (Kaede$^{PC}$) 15 hr later (32 hpf). Whereas Kaede$^{PC}$ cells inhabited both the heart and the pharyngeal arches in control animals (Figures 3K and 3L), labeled cells were present only in the hearts of *tbx1* mutants (Figures 3M and 3N). Taken together, these data demonstrate that Tbx1 functions to specify the *nkx2.5*$^{+}$ pharyngeal progenitor lineage in zebrafish. They also suggest that the *nkx2.5*$^{+}$ pharyngeal progenitor lineage is normally specified prior to the cardiac lineage. However, it is equally possible that the lineages are co-specified in wild-type embryos, and the phenotype we observe (Figures 3A–3H) results from delayed cardiac lineage specification in *tbx1* mutants.

## *nkx2.5*$^{+}$ Progenitors in the ALPM of Zebrafish Embryos Co-express *tbx1*

Next, we examined *tbx1* expression at stages surrounding the onset of *nkx2.5* transcription to learn whether it initiates first and whether it might overlap with *nkx2.5* in the ALPM. We detected *tbx1* expression preceding that of *nkx2.5* at the tail bud stage in a broad bilateral pattern (Figure 4A). A similar expression pattern was observed at 2 ss (Figure 4B), when *nkx2.5* transcripts first appear (Figure 3A). Thereafter, *tbx1* coalesces into

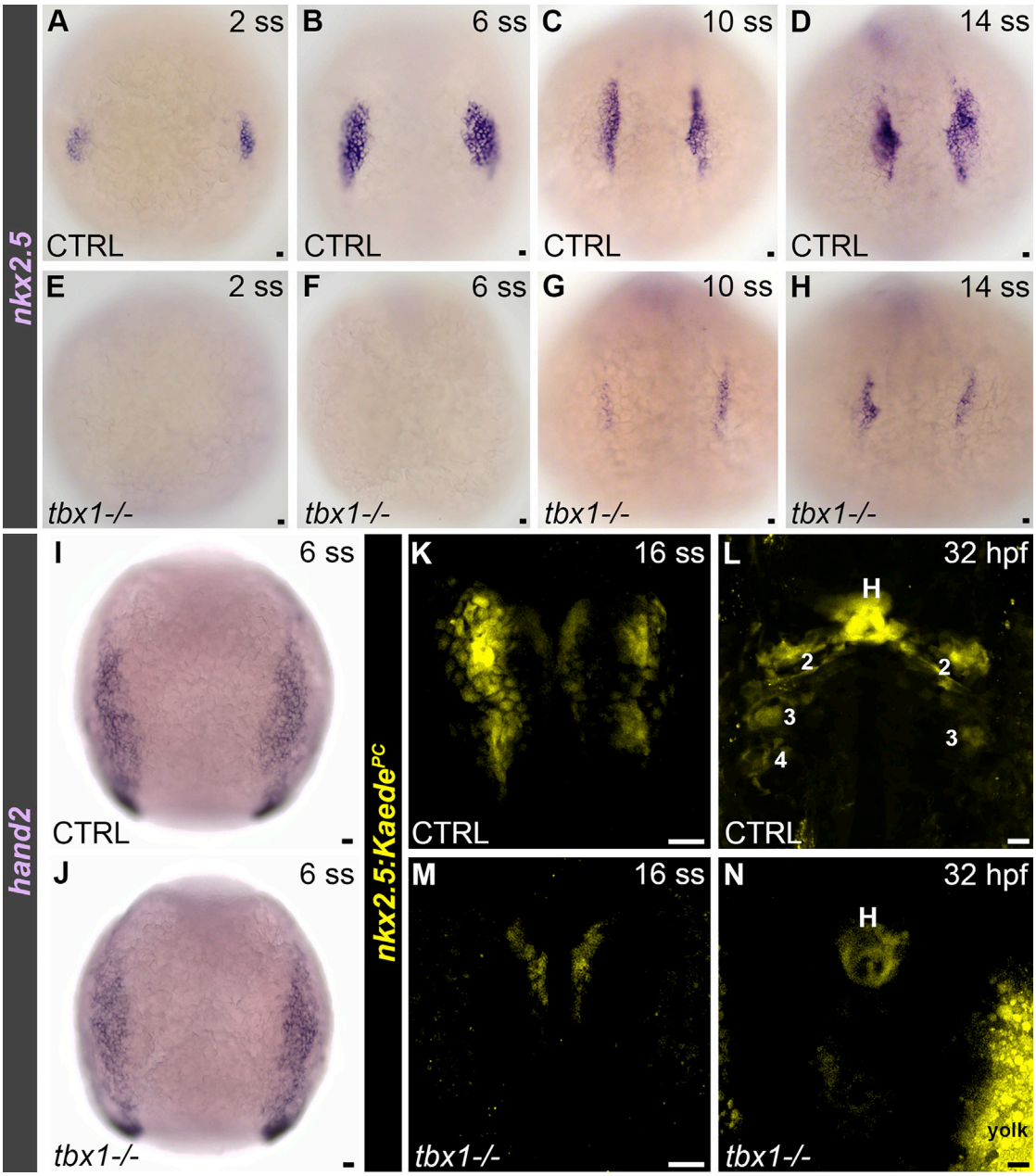


**Figure 3. Tbx1 Is Required for Specification of the *nkx2.5*$^{+}$ Pharyngeal Lineage in the ALPM of Zebrafish Embryos**

(A–H) Bright-field images of 2 somite stage (ss) (A, n = 30; E, n = 10), 6 ss (B, n = 60; F, n = 20), 10 ss (C, n = 30; G, n = 11), and 14 ss (D, n = 10; H, n = 10) control (CTRL) (A–D) and *tbx1* mutant (E–H) embryos processed by *in situ* hybridization with an *nkx2.5* riboprobe. Dorsal views, anterior up.

(I and J) Bright-field z-stacks of 6 ss CTRL (I; n = 42) and *tbx1* mutant (J; n = 13) embryos processed by *in situ* hybridization with a *hand2* riboprobe. Dorsal views, anterior up.

(K–N) Confocal z-stacks of CTRL (K and L) and *tbx1* mutant (M and N) *Tg(nkx2.5:Kaede)* embryos imaged immediately following photoconversion at the 16 ss (K and M) and again at 32 hr post-fertilization (L and N). Four of four CTRL embryos contained photoconverted Kaede protein (Kaede$^{PC}$, pseudocolored yellow) in the heart and pharyngeal clusters at 32 hpf. Four of four mutant embryos contained Kaede$^{PC}$ exclusively in the heart. Dorsal views, anterior up.

In (A)–(K), little to no variation was observed between animals in each experimental group.

Scale bars, 25 μm.

taller lateral and shorter medial expression domains (Figures 4C and 4D). Studies in *Ciona intestinalis* have revealed that bipotential cardiopharyngeal progenitor cells co-express homologs of *Tbx1* and *Nkx2.5* prior to their segregation into cardiac and pharyngeal lineages (Wang et al., 2013). To determine whether *nkx2.5*$^{+}$ progenitor cells in the zebrafish ALPM co-express

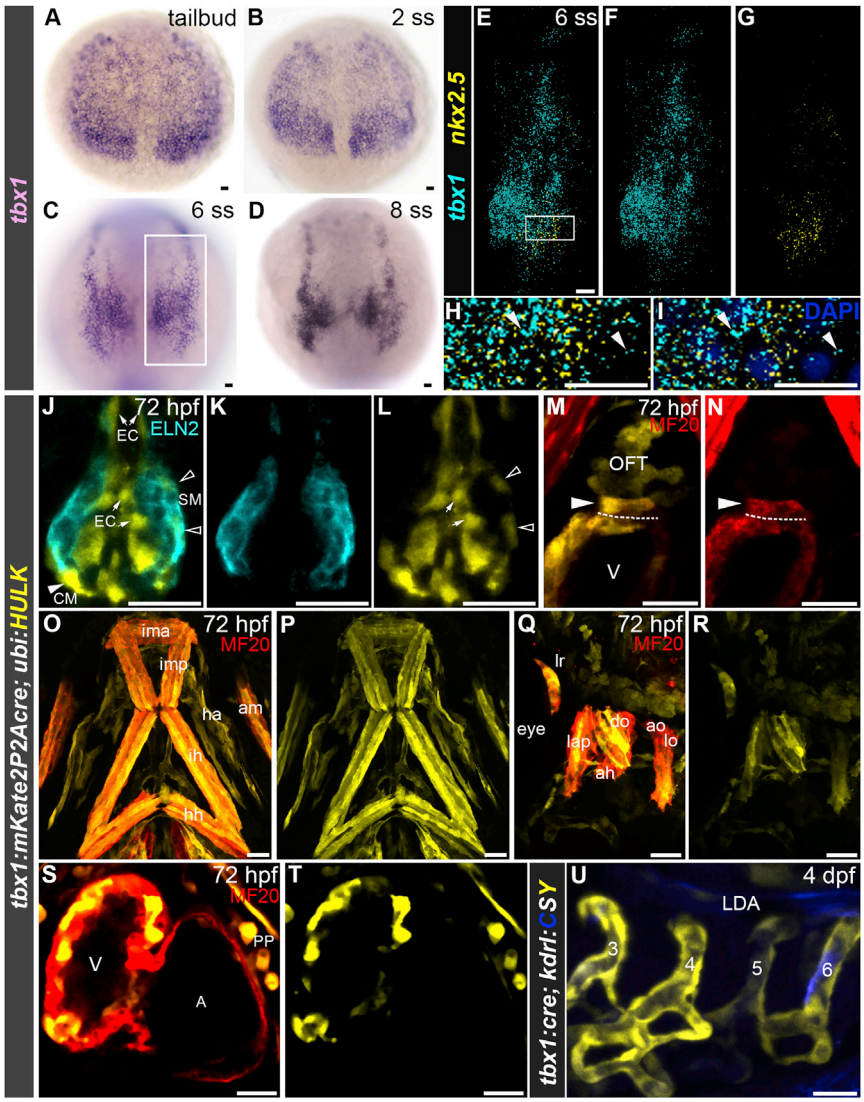


**Figure 4. *nkx2.5*$^+$ Progenitors in the ALPM of Zebrafish Embryos Co-express *tbx1***

(A–D) Bright-field images of wild-type embryos (n = 15 per stage) between tail bud and 8 somite stage (ss) processed by *in situ* hybridization with a *tbx1* riboprobe. Boxed area in (C) shows region of embryo analyzed in (E)–(G). Dorsal views, anterior up.

(E–I) Confocal z-stack of the *tbx1* and *nkx2.5* expression domains on the right side of a 6 ss wild-type embryo (n = 14) processed by RNAscope double-fluorescent *in situ* hybridization with *tbx1* (pseudocolored cyan) and *nkx2.5* (pseudocolored yellow) riboprobes. Merged double- (E) and single-channel (F and G) images are shown. Projection of selected z-stack images from the boxed region in (E) is shown at higher magnification in (H). A single section from (H) is shown in (I) (arrowheads are shown to indicate regions of overlap) with DAPI nuclei counterstaining. Dorsal views, anterior up.

(J–T) Single optical sections (J–N, S, T) or confocal z-stacks (O–R) of the OFT (J–N), PA1- and PA2-derived HMs (O–R), and heart (S and T) in a 72 hpf *Tg(tbx1:mKate2P2Acre)*, *Tg(ubi:HULK)* double-transgenic embryo co-immunostained with antibodies recognizing GFP (pseudocolored yellow) and OFT smooth muscle (Eln2; J–L; pseudocolored cyan, n = 15) or GFP (pseudocolored yellow) and striated muscle (MF20; M–T; red, n = 39) antibodies. Arrows, open arrowheads, and closed arrowheads point to GFP$^+$ OFT endothelial cells (EC), OFT smooth muscle cells (SM), and OFT cardiomyocytes (CM) in (J), (L), and (M), respectively. Dashed lines demarcate the boundary between the ventricular and OFT myocardium in (M) and (N). Ventral views, anterior up (J–P, S, T). Lateral view, anterior left (Q and R). Merged (J, M, O, Q, S) and single (K, L, N, P, R, T)-channel images are shown.

(U) Confocal z-stack of a 4 days post-fertilization (dpf) *Tg(tbx1:mKate2P2Acre); Tg(kdrl:CSY)* double-transgenic embryo (n = 22) showing expression of AmCyan and ZsYellow from the unrecombined and recombined reporter, respectively. Lateral view, anterior to the left. The numbers identify each PAA.

In (J)–(N and (S)–(U), all of the animals contained some reporter expression in the structures shown, but the distribution within each structure was variable. In (O) and (P), little to no variation was observed in head muscle labeling between animals. In (A)–(I), little to no variation was observed between animals in each experimental group.

Scale bars, 25 μm. PA1-derived head muscles: am, abductor mandibulae; do, dilator operculi; ima, intermandibularis anterior; imp, intermandibularis posterior; lap, levator arcus palatini; PA2-derived head muscles: ah, adductor hyoideus; ao, adductor operculi; ha, hypobranchial artery; hh, hyohyoidus; ih, interhyoidus; lo, levator operculi; lr, lateral rectus ocular muscle. A, atrium; LDA, lateral dorsal aorta; OFT, outflow tract; PP, parietal pericardium; V, ventricle.

*tbx1*, we performed double-fluorescent *in situ* hybridization using RNAscope technology at 6 ss. Examination of confocal projections revealed that the entire *nkx2.5* expression domain resides posteriorly and laterally within the *tbx1* expression domain (Figures 4E–4G). We confirmed the double positivity of these cells (Figure 4H) by visualizing both transcripts overlapping individual nuclei in single confocal sections (Figure 4I). Together, these data demonstrate that the earliest *nkx2.5*$^+$ progenitors in the ALPM co-express *tbx1*.

To provide complementary evidence for this conclusion, we created a transgenic strain co-expressing mKate2 and Cre recombinase from *tbx1* *cis*-regulatory elements [*Tg(tbx1:mKate2P2Acre)*, abbreviated *Tg(tbx1:cre)*], and confirmed that the pattern of mKate2 fluorescence recapitulated that of endogenous *tbx1* transcripts (Figure S2). If ALPM progenitors co-express *nkx2.5* and *tbx1*, then the same structures derived from *nkx2.5*$^+$ progenitors, including ventricular myocardium, PAA endothelium, PA1- and PA2-derived HMs, and OFT lineages should also be labeled in a *tbx1* lineage trace. Therefore, we created double-transgenic embryos carrying *Tg(tbx1:cre)* and Cre-responsive ubiquitous [*Tg(ubi:HULK)*] or endothelial-specific [*Tg(kdrl:CSY)*] color-switching transgenes and analyzed embryos for reporter fluorescence at 72 hpf. We documented reporter fluorescence in three OFT lineages

(Figures 4J–4N), PA1- and PA2-derived HMs (Figures 4O–4R), ventricular myocardium (Figures 4S and 4T), and PAA endothelium (Figure 4U). Additionally, the parietal pericardium (Figures 4S, 4T, S3A, and S3B) and multiple head tissues, including cranial vessels (Figures S3A and S3C), ocular vessels (Figures S3A and S3D), and extraocular muscles (Figures 4Q, S3A, and S3D) were labeled. Overall, these data support the conclusion that *nkx2.5*$^{+}$ progenitors in the ALPM of zebrafish embryos co-express *tbx1*.

### *gdf3* is Downstream of *tbx1* during Specification of *nkx2.5*$^{+}$ Pharyngeal Progenitors

Next, we identified candidate downstream mediators of *tbx1*-dependent *nkx2.5*$^{+}$ pharyngeal lineage specification by comparing the transcriptomes of *tbx1* mutant embryos with their wild-type siblings at 6 ss by RNA sequencing. Among a relatively small number of transcripts (270) showing statistically significant ($p < 0.05$) fold changes in *tbx1* mutants (Figure S4), those encoding Gdf3, the single zebrafish ortholog of mammalian TGFβ superfamily ligands GDF1 and GDF3 (Andersson et al., 2007; Bisgrove et al., 2017; Dohrmann et al., 1996; Helde and Grunwald, 1993; Montague and Schier, 2017; Pelliccia et al., 2017; Peterson et al., 2013), were identified as significantly downregulated (Figure S4). We prioritized *gdf3* for further study because patients harboring *GDF1* mutations display cardiovascular anomalies similar to those present in the 22q11DS population (Jin et al., 2017; Karkera et al., 2007). As expected, *tbx1* and *nkx2.5* transcripts were also identified as significantly reduced in *tbx1* mutants (Figure S4). Using qPCR, we corroborated that *gdf3, tbx1*, and *nkx2.5* transcripts are all reduced in 6 ss *tbx1* mutants (Figure 5A).

We localized *gdf3* expression by *in situ* hybridization to bilateral stripes in the anterior region of 6 ss control embryos (Figure 5B). As anticipated, expression was highly reduced in *tbx1* mutants (Figure 5C), demonstrating that *gdf3* lies genetically downstream of *tbx1* during pharyngeal progenitor specification. Nonetheless, overexpression of *gdf3* mRNA failed to rescue *nkx2.5* expression in the ALPM of *tbx1* mutants at 6 ss (Figures S5A–S5F), suggesting that additional factors are required. Using RNAscope technology, we performed triple *in situ* hybridization for *gdf3, tbx1*, and *nkx2.5*, and learned that *gdf3* expression is positioned lateral to that of *tbx1* (Figures 5D, 5E, 5G, and 5H). However, overlap between the two expression domains existed posteriorly in cells that were triple positive for *gdf3*, *tbx1*, and *nkx2.5* (Figures 5D–5I). We confirmed the triple positivity of these cells (Figure 5J) by visualizing all three transcripts overlapping individual nuclei in single confocal sections (Figure 5K). This triple-positive population appeared to encompass all of the *nkx2.5*$^{+}$ progenitors in the ALPM (Figures 5D and 5F–5I).

To determine whether *gdf3* might be mediating *tbx1*-dependent specification of the *nkx2.5*$^{+}$ pharyngeal lineage, we used CRISPR/Cas9-mediated genome editing to create a *gdf3* null allele. We isolated a 10-bp deletion in exon 2 (Δ5′-TGGAG GAAAC-3′) that shifts the open reading frame and creates a premature stop codon upstream of the mature ligand domain (Figure 5L). Zygotic deletion of *gdf3* (*Zgdf3*) resulted in mutant embryos that were indistinguishable from control siblings with respect to whole-body morphology (Figures 5M and 5N), PAA (Figures S6A and S6B), HM (Figures S6D, S6E, S6G, and S6H), and OFT development (Figures S6D and S6E), and *nkx2.5* expression in the ALPM (Figures S6J and S6K). These animals survived to adulthood and produced offspring. The absence of a gross zygotic phenotype might be explained by high levels of maternally deposited *gdf3* mRNA and protein (Dohrmann et al., 1996; Helde and Grunwald, 1993). Therefore, we incrossed *gdf3* null animals to create embryos lacking both maternal and zygotic sources of Gdf3 (MZ*gdf3*). At 28 hpf, these animals appeared to lack both head and trunk mesoderm (Figure 5O), a phenotype closely resembling that of *nodal* pathway mutants (Gritsman et al., 1999). Recently, three studies documented a lack of head and trunk mesendodermal lineages in MZ*gdf3* mutants isolated independently (Bisgrove et al., 2017; Montague and Schier, 2017; Pelliccia et al., 2017). Accordingly, analysis of our MZ*gdf3* animals revealed a complete lack of PAA angioblasts (Figures S6A and S6C), HMs (Figures S6D, S6F, S6G, and S6I), and OFTs (Figures S6D and S6F), as well as *nkx2.5* expression in the ALPM (Figures S6J and S6L), which precluded us from assessing the specific role of *gdf3* in *nkx2.5*$^{+}$ pharyngeal lineage specification.

### Small-Molecule-Mediated Inhibition of the Gdf3 Receptor Alk4 Phenocopies the Pharyngeal and *nkx2.5*$^{+}$ Progenitor Specification Defects Observed in *tbx1* Mutants

As a means of circumventing this experimental barrier, we employed a small molecule (SB-505124) to antagonize the Gdf3 type I receptor Alk4 (Bisgrove et al., 2017; Cheng et al., 2003). Continuous treatment of wild-type embryos with SB-505124 prior to gastrulation (4 hpf) resulted in a gross embryonic phenotype similar to that of MZ*gdf3* mutants (Figure S7), suggesting that the small molecule antagonizes the Gdf3 receptor. To learn whether Alk4 inhibition elicits similar pharyngeal phenotypes to those observed in *tbx1* mutants, we treated embryos with SB-505124 between 75% epiboly and 24 hpf (Figure 6A), a developmental window subsequent to mesoderm induction that overlaps *nkx2.5*$^{+}$ pharyngeal progenitor specification (Figures 3A–3D). After chemical washout, embryos were allowed to develop further and were binned into classes based on PAA angioblast, HM, and OFT phenotypes (Figure 6A). Dose-dependent reductions were observed in *tie1*$^{+}$ PAA angioblasts at 38 hpf (Figures 6B–6E), PA1- and PA2-derived HMs at 72 hpf (Figures 6F–6L), and OFT smooth muscle at 72 hpf (Figures 6F–6H and 6M), all of which are phenotypes shared by *tbx1* mutants (Figures 1E–1L).

To learn whether these deficiencies could be attributed to compromised pharyngeal lineage specification as observed in *tbx1* mutants (Figures 3E and 3F), we suppressed Alk4 signaling after mesoderm induction (75% epiboly, 8 hpf) and assessed 6 ss animals for *nkx2.5* expression by *in situ* hybridization. SB-505124-treated embryos displayed reductions in the size or loss of the *nkx2.5* expression domain (Figures 7A–7D), suggesting that specification of the pharyngeal progenitor cell lineage is compromised. However, no decrease in the *tbx1* expression domain size was observed (Figures 7E–7H). Together, these data support a model in which *gdf3*-Alk4 signaling mediates *tbx1*-dependent specification of *nkx2.5*$^{+}$ pharyngeal progenitor cells.

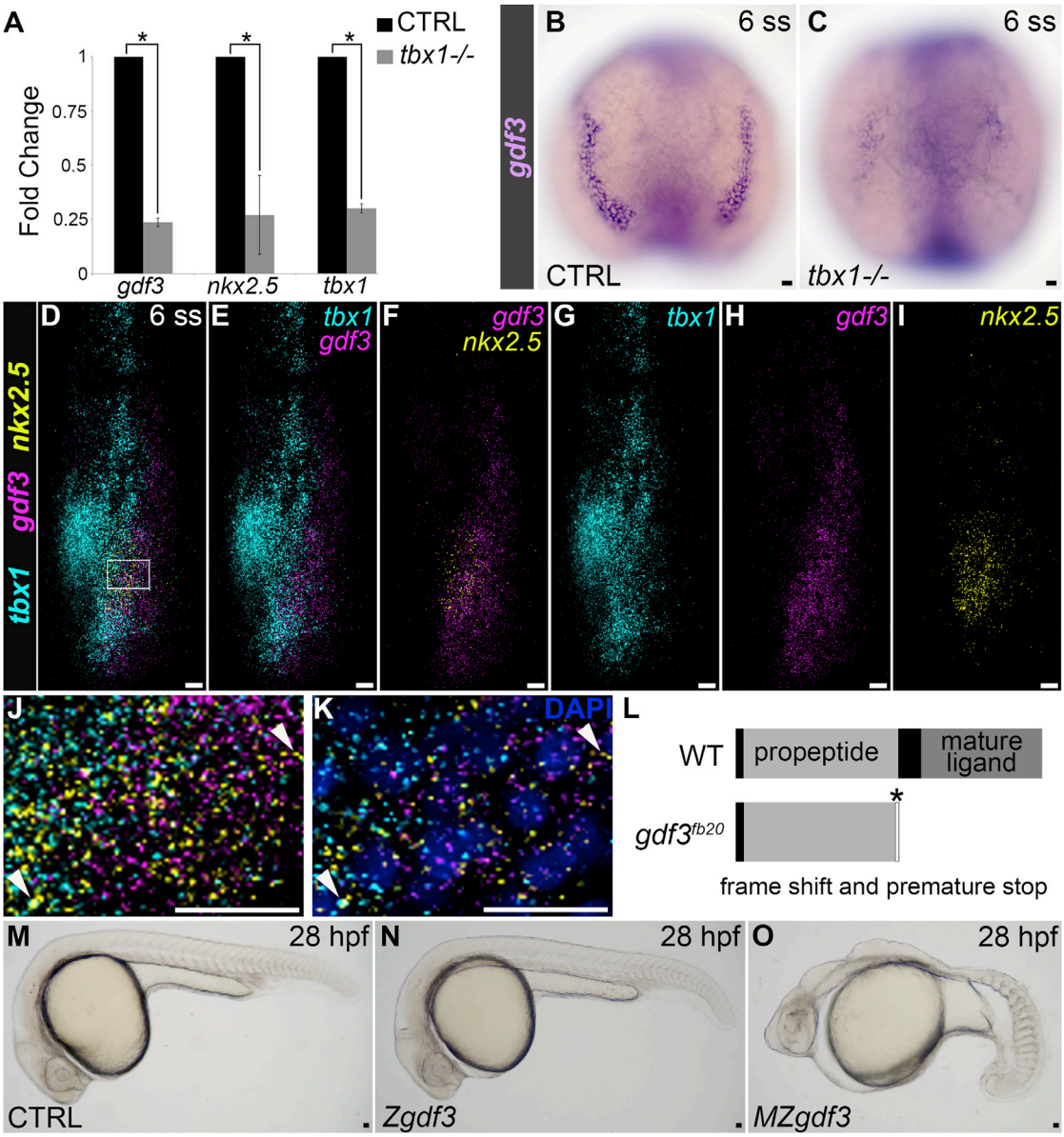


**Figure 5. *gdf3* Is Downstream of *tbx1* during Specification of *nkx2.5*$^{+}$ Pharyngeal Progenitors**

(A) Bar graph showing the relative expression levels of *gdf3*, *nkx2.5*, and *tbx1* transcripts in 6 somite stage (ss) control (CTRL) and *tbx1* mutant embryos measured by qPCR. Three biological replicates were analyzed. Error bars show SD. *$p < 0.05$ as determined by an unpaired two-tailed t test.

(B and C) Bright-field images of 6 ss CTRL (B; n = 40) and *tbx1* mutant (C; n = 12) embryos processed by *in situ* hybridization with a *gdf3* riboprobe. Dorsal views, anterior up.

(D–I) Confocal z-stacks of the *tbx1*, *gdf3*, *and nkx2.5* expression domains on the right side of a 6 ss wild-type zebrafish embryo (n = 7) processed by RNAscope triple-fluorescent *in situ* hybridization with *tbx1* (pseudocolored cyan), *gdf3* (pseudocolored magenta), and *nkx2.5* (pseudocolored yellow) riboprobes. Merged triple- (D), double- (E and F), and single- (G–I) channel images are shown.

(J) Projection of selected z-stack images from the boxed region in (D) is shown at higher magnification.

(K) A single confocal section from (J) is shown in (K) (arrowheads are shown to indicate regions of overlap) with DAPI nuclei counterstaining.

(L) Schematic diagrams showing the domain structures of the predicted protein products of wild-type (WT) *gdf3* and a null allele of *gdf3*, *gdf3*$^{fb20}$, generated by CRISPR/Cas9-mediated genome editing. The asterisk highlights the location of a frameshifting 10-bp deletion in the *gdf3*$^{fb20}$ mRNA, which causes the translation of six ectopic amino acids (white) before a premature stop codon truncates the protein upstream of the mature ligand domain.

(M–O) Bright-field z-stacks of live 28 hr post-fertilization (hpf) CTRL (M; n = 25), zygotic *gdf3* (N; *Zgdf3*, n = 25), and maternal-zygotic *gdf3* (O; MZ*gdf3*, n = 40) zebrafish embryos. Lateral views, anterior left.

In all cases, little to no variation was observed between animals in each experimental group. Scale bars, 25 μm.

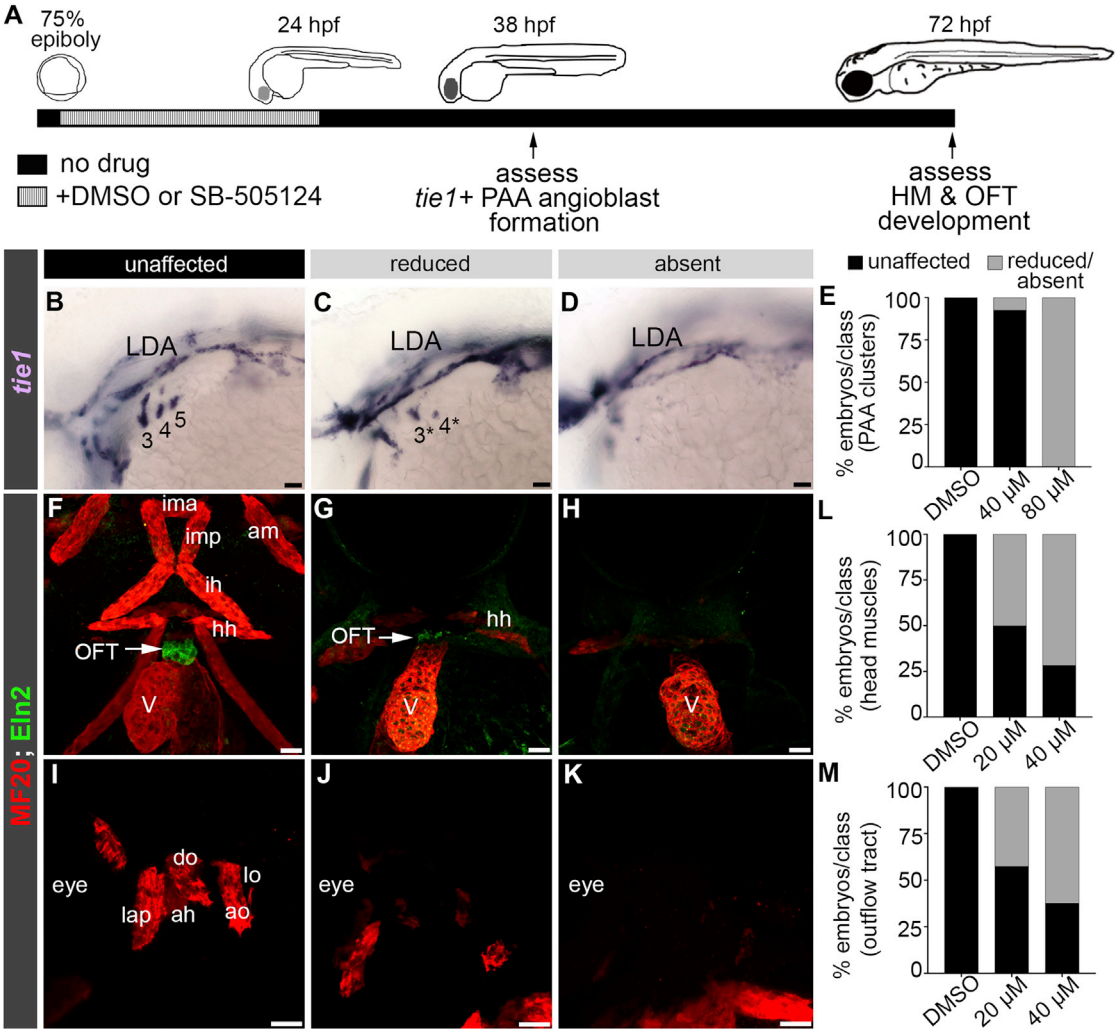


**Figure 6. Small-Molecule-Mediated Inhibition of the Gdf3 Receptor Alk4 Phenocopies the Pharyngeal Defects Observed in *tbx1* Mutants**

(A) Experimental timeline of SB-505124 treatment and phenotypic analyses.

(B–D) Bright-field z-stacks of 38 hr post-fertilization (hpf) wild-type embryos treated with DMSO or SB-505124 between 75% epiboly and 24 hpf, and processed by *in situ* hybridization with a *tie1* riboprobe. Images of representative animals with unaffected (B; 3 or more clusters), reduced (C; 1–2 clusters), or absent (D; 0 clusters) *tie1*$^{+}$ pharyngeal arch artery (PAA) clusters are shown. The numbers in (B) and (C) identify each PAA cluster. The asterisks highlight clusters of smaller size in (C). Lateral views, anterior left.

(E) Bar graph showing the percentages of embryos with unaffected, reduced, or absent PAA clusters after treatment with DMSO (n = 22), 40 μM SB-505124 (n = 27), or 80 μM SB-505124 (n = 12).

(F–K) Confocal z-stacks of 72 hpf wild-type embryos treated between 75% epiboly and 24 hpf with DMSO or SB-505124 and co-immunostained with antibodies recognizing striated muscle (MF20, red) or outflow flow tract (OFT) smooth muscle (Eln2, green). Images of representative animals with unaffected (F and I), reduced (G and J), or absent (H and K) head muscles and OFTs (white arrows, F and G) are shown. (F–H) Ventral views, anterior up. (I–K) Lateral views, anteior left.

(L and M) Bar graphs showing the percentages of animals with unaffected, reduced, or absent head muscles (L) or OFTs (M) after treatment with DMSO (n = 49), 20 μM SB-505124 (n = 40), or 40 μM SB-505124 (n = 53).

Scale bars, 25 μm. PA1-derived head muscles: am, abductor mandibulae; do, dilator operculi; ima, intermandibularis anterior; imp, intermandibularis posterior; lap, levator arcus palatini; PA2-derived head muscles: ah, adductor hyoideus; ao, adductor operculi; hh, hyohyoidus; ih, interhyoidus; lo, levator operculi. LDA, lateral dorsal aorta. OFT, outflow tract; V, ventricle.

## DISCUSSION

Our findings demonstrate that Tbx1 plays a primary role in cardiovascular and craniofacial development prior to pharyngeal arch morphogenesis in zebrafish. Specifically, we report that Tbx1 functions during early somatogenesis to specify the *nkx2.5*$^{+}$ pharyngeal progenitor cell lineage, which gives rise to the structures disrupted in *tbx1* mutant embryos including the PAAs, PA2-derived HMs, and OFT. Furthermore, we identify *gdf3* as genetically downstream of *tbx1* and demonstrate that signaling through its receptor Alk4 is required for *nkx2.5*$^{+}$ pharyngeal lineage specification.

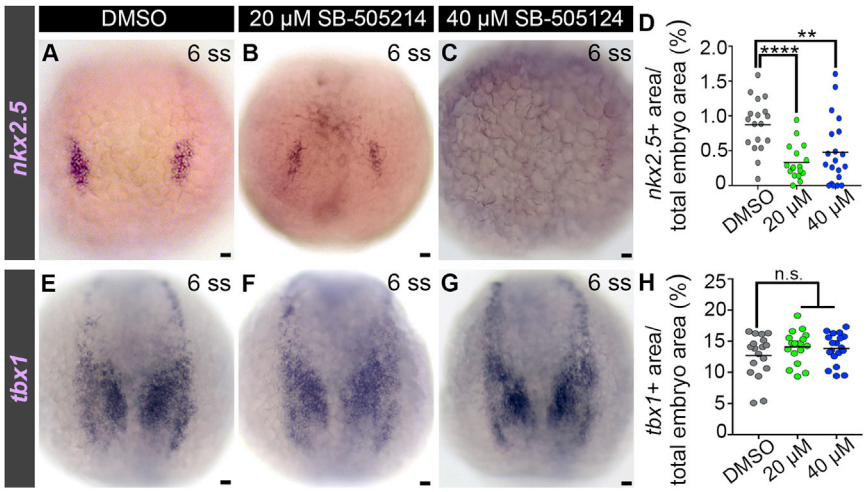


**Figure 7. Small-Molecule-Mediated Inhibition of the Gdf3 Receptor Alk4 Phenocopies the *nkx2.5*$^+$ Progenitor Specification Defect Observed in *tbx1* Mutants**

(A–C) Bright-field images of 6 somite stage (ss) wild-type embryos processed by *in situ* hybridization with an *nkx2.5* riboprobe after being treated from 75% epiboly with DMSO (A; n = 18), 20 μM SB-505124 (B; n = 17), or 40 μM SB-505124 (C; n = 20). Dorsal views, anterior up.

(D) Dot plot showing the average sizes of the bilateral *nkx2.5* expression domain, normalized to the total embryo area shown in each image, in each experimental group. **p < 0.01; ****p < 0.0001, as determined by one-way ANOVA followed by Tukey's multiple comparisons test.

(E–G) Bright-field images of 6 ss wild-type embryos processed by *in situ* hybridization with a *tbx1* riboprobe after being treated with DMSO (E; n = 18), 20 μM SB-505124 (F; n = 18), or 40 μM SB-505124 (G; n = 19) beginning at 75% epiboly. Dorsal views, anterior up.

(H) Dot plot showing the average sizes of the bilateral *tbx1* expression domain, normalized to the total embryo area shown in each image, in each experimental group. n.s., nonsignificant as determined by a one-way ANOVA test.

Scale bars, 25 μm.

On a cellular level, Tbx1 has been previously implicated in promoting proliferation and inhibiting differentiation of cardiovascular progenitor cells (Chen et al., 2009). Our study highlights an unappreciated role for Tbx1 in specifying the *nkx2.5*$^+$ pharyngeal progenitor cell fate in zebrafish. Whether Tbx1 performs a similar cellular function in mammals remains to be determined. However, parallels can be drawn between the zebrafish and mouse in this regard. Both zebrafish and mouse *Tbx1* mutants display PAA, PA2-derived HM, and OFT deficiencies, suggesting that the function of Tbx1 in cardiopharyngeal development is conserved across species. The *nkx2.5*$^+$ lineages in both species seed the mesodermal cores of the pharyngeal arches (Paffett-Lugassy et al., 2013; Zhang et al., 2005) and give rise to PAA endothelium (Paffett-Lugassy et al., 2013), PA2-derived HMs (Harel et al., 2009; Paffett-Lugassy et al., 2017), OFT myocardium (Stanley et al., 2002), and smooth muscle (Harmon and Nakano, 2013). Although *Nkx2.5* expression has not been measured in the ALPM or pharyngeal arches of *Tbx1* mutant mice, a transgenic reporter of *FGF10* expression, which labels core mesoderm, PAA endothelium, and the OFT, was shown to be reduced or absent at E8.5–E10.5 (Kelly and Papaioannou, 2007). Even though these observations are consistent with *Tbx1* performing an indispensable role in specifying the pharyngeal lineage in mouse, an examination of *Nkx2.5* expression in the ALPM of *Tbx1* mutant animals will be required to further investigate this hypothesis. If failed progenitor specification underlies the cardiopharyngeal defects observed in mammals, including humans, then the wide variation in disease phenotypes observed in the 22q11.2DS population might reflect the influence of modifiers over the number of pharyngeal progenitor cells specified during early embryonic life.

The molecular mechanism(s) by which Tbx1 regulates pharyngeal lineage specification also remains unclear. Although historically considered to be a transcription factor (Scambler, 2010), Tbx1 was recently reported to alter chromatin accessibility through histone methyltransferase recruitment and H3K4me1 deposition (Fulcoli et al., 2016). Therefore, in addition to regulating transcription directly, Tbx1 might also function as a chromatin priming factor by balancing methylation levels at target enhancers such that they remain poised for cell-type-specific transcriptional modulation. Additional studies will be required to learn whether Tbx1 controls pharyngeal lineage determination through one or both of these mechanisms.

Our data also provide further support to the emerging notion that pharyngeal segmentation phenotypes observed in *tbx1*-deficient mice and zebrafish are secondary to the loss of critical signals from pharyngeal mesoderm (Choe et al., 2013; Choe and Crump, 2014; Zhang et al., 2006). This idea is supported by the observation that genetic ablation of mesodermal *nkx2.5*$^+$ cells in wild-type zebrafish is sufficient to elicit pharyngeal segmentation defects (Choe et al., 2013). Similarly, deletion of Tbx1 specifically from the mesoderm undermines pharyngeal segmentation during mouse development (Zhang et al., 2006). Moreover, re-expression of *Tbx1* in the pharyngeal mesoderm of *Tbx1* mutant zebrafish or mice partially restores endodermal pouch outgrowth (Choe and Crump, 2014; Zhang et al., 2006). In zebrafish, Fgf8a and Wnt11r mediate the crosstalk between pharyngeal mesoderm and endoderm because restoring their expression in the pharyngeal mesoderm of *tbx1* mutants is sufficient to partially rescue pouch formation (Choe and Crump, 2014). Our studies extend these observations by demonstrating that the reported absence of *fgf8a* and *wnt11r* in the pharyngeal mesoderm of *tbx1* mutants (Choe and Crump, 2014) can be attributed to loss of the entire *nkx2.5*$^+$ pharyngeal lineage. Ultimately, our studies provide a unifying cellular mechanism that explains both the pharyngeal (PAAs, HMs, and OFT) and segmentation phenotypes in *tbx1* mutant zebrafish.

## STAR★METHODS

Detailed methods are provided in the online version of this paper and include the following:

- KEY RESOURCES TABLE
- CONTACT FOR REAGENT AND RESOURCE SHARING
- EXPERIMENTAL MODEL AND SUBJECT DETAILS
- METHOD DETAILS
  - Zebrafish Whole Mount Immunohistochemistry
  - Zebrafish Whole Mount *In Situ* Hybridization
  - RNAscope Whole Mount *In Situ* Hybridization
  - Kaede Photoconversion
  - Generation of The Tg(tbx1:mKate2P2Acre) and Tg(tbx1:GFP) Lines
  - TUNEL Staining
  - Zebrafish Lineage Tracing
  - RNA-Sequencing and Library Preparation
  - RNA-Seq Data Processing
  - *gdf3* (*vg1*) mRNA Synthesis
  - Generation of a *gdf3* Null Allele by CRISPR-Cas9 Genome Editing
  - Gdf3 Mutant Genotyping
  - Small Molecule Treatment
- QUANTIFICATION AND STATISTICAL ANALYSIS
- DATA AND SOFTWARE AVAILABILITY

## SUPPLEMENTAL INFORMATION

Supplemental Information includes seven figures and can be found with this article online at https://doi.org/10.1016/j.celrep.2018.06.117.

## ACKNOWLEDGMENTS

We are grateful to B. Barut and L. Zon for providing bacterial artificial chromosomes (BACs), T. Evans for providing *nkx2.5* plasmid for probe generation, and N. Mercader Huber for providing the *Tg(ubi:HULK)* reporter strain. B.G.-A. was supported by the American Heart Association Scientist Development Grant (14SDG19020018). J.M.G.-R. received support from an EMBO Long-Term Fellowship (ALTF 253-2014) and a Fund for Medical Discovery award from the Executive Committee on Research at Massachusetts General Hospital. H.N.S. was supported by the Howard Hughes Medical Institute Medical Research Fellows Program. M.A. was supported by a Servier Institute International Mobility Help Grant and a Victor A. McKusick Fellowship from the Marfan Foundation (2016D001458). The BioMicro Center at MIT that performed the RNA sequencing and the bioinformatics was funded by the NIH National Cancer Institute under award P30-CA14051. L.A.B. was supported by the American Heart Association (15GRNT25670044). This work was supported by an R01 award (R01HL096816) from the NIH (to C.G.B.), by the Children's Heart Foundation (to C.E.B.), and by an R35 award (R35HL135831) from the NIH (to C.E.B.). C.G.B. is supported by an MGH Hassenfeld Cardiovascular Scholar award, and C.E.B. is supported by a d'Arbeloff MGH Research Scholar Award.

## AUTHOR CONTRIBUTIONS

B.G.-A. designed and performed experiments, analyzed data, and co-wrote the paper; J.M.G.-R. and M.A. designed, performed, and analyzed zebrafish experiments; S.J. and H.N.S. performed and analyzed zebrafish experiments; V.L.B. and L.A.B. performed bioinformatics analysis; C.G.B. and B.G.-A. created the *Tg(tbx1:mKate2P2Acre)* and *Tg(tbx1:GFP)* lines; C.G.B. and C.E.B. initiated and directed the study, analyzed data, and co-wrote the paper with input from all authors.

## DECLARATION OF INTERESTS

The authors declare no competing interests.

Received: November 14, 2017
Revised: May 8, 2018
Accepted: June 28, 2018
Published: July 31, 2018

## REFERENCES

Abrial, M., Paffett-Lugassy, N., Jeffrey, S., Jordan, D., O'Loughlin, E., Frederick, C.J., 3rd, Burns, C.G., and Burns, C.E. (2017). TGF-β signaling is necessary and sufficient for pharyngeal arch artery angioblast formation. Cell Rep. *20*, 973–983.

Anderson, M.J., Pham, V.N., Vogel, A.M., Weinstein, B.M., and Roman, B.L. (2008). Loss of unc45a precipitates arteriovenous shunting in the aortic arches. Dev. Biol. *318*, 258–267.

Andersson, O., Bertolino, P., and Ibáñez, C.F. (2007). Distinct and cooperative roles of mammalian Vg1 homologs GDF1 and GDF3 during early embryonic development. Dev. Biol. *311*, 500–511.

Arnold, J.S., Werling, U., Braunstein, E.M., Liao, J., Nowotschin, S., Edelmann, W., Hebert, J.M., and Morrow, B.E. (2006). Inactivation of Tbx1 in the pharyngeal endoderm results in 22q11DS malformations. Development *133*, 977–987.

Bisgrove, B.W., Su, Y.-C., and Yost, H.J. (2017). Maternal Gdf3 is an obligatory cofactor in Nodal signaling for embryonic axis formation in zebrafish. Elife *6*, e28534.

Botto, L.D., May, K., Fernhoff, P.M., Correa, A., Coleman, K., Rasmussen, S.A., Merritt, R.K., O'Leary, L.A., Wong, L.-Y., Elixson, E.M., et al. (2003). A population-based study of the 22q11.2 deletion: phenotype, incidence, and contribution to major birth defects in the population. Pediatrics *112*, 101–107.

Chen, L., Fulcoli, F.G., Tang, S., and Baldini, A. (2009). Tbx1 regulates proliferation and differentiation of multipotent heart progenitors. Circ. Res. *105*, 842–851.

Cheng, S.K., Olale, F., Bennett, J.T., Brivanlou, A.H., and Schier, A.F. (2003). EGF-CFC proteins are essential coreceptors for the TGF-beta signals Vg1 and GDF1. Genes Dev. *17*, 31–36.

Choe, C.P., and Crump, J.G. (2014). Tbx1 controls the morphogenesis of pharyngeal pouch epithelia through mesodermal Wnt11r and Fgf8a. Development *141*, 3583–3593.

Choe, C.P., Collazo, A., Trinh, A., Pan, L., Moens, C.B., and Crump, J.G. (2013). Wnt-dependent epithelial transitions drive pharyngeal pouch formation. Dev. Cell *24*, 296–309.

Choi, J., Dong, L., Ahn, J., Dao, D., Hammerschmidt, M., and Chen, J.-N. (2007). FoxH1 negatively modulates flk1 gene expression and vascular formation in zebrafish. Dev. Biol. *304*, 735–744.

Di Donato, V., De Santis, F., Auer, T.O., Testa, N., Sánchez-Iranzo, H., Mercader, N., Concordet, J.-P., and Del Bene, F. (2016). 2C-Cas9: a versatile tool for clonal analysis of gene function. Genome Res. *26*, 681–692.

Dohrmann, C.E., Kessler, D.S., and Melton, D.A. (1996). Induction of axial mesoderm by zDVR-1, the zebrafish orthologue of Xenopus Vg1. Dev. Biol. *175*, 108–117.

Fulcoli, F.G., Franzese, M., Liu, X., Zhang, Z., Angelini, C., and Baldini, A. (2016). Rebalancing gene haploinsufficiency in vivo by targeting chromatin. Nat. Commun. *7*, 11688.

Graham, A. (2003). Development of the pharyngeal arches. Am. J. Med. Genet. A. *119A*, 251–256.

Gritsman, K., Zhang, J., Cheng, S., Heckscher, E., Talbot, W.S., and Schier, A.F. (1999). The EGF-CFC protein one-eyed pinhead is essential for nodal signaling. Cell *97*, 121–132.

Gross-Thebing, T., Paksa, A., and Raz, E. (2014). Simultaneous high-resolution detection of multiple transcripts combined with localization of proteins in whole-mount embryos. BMC Biol. *12*, 55.

Guner-Ataman, B., Paffett-Lugassy, N., Adams, M.S., Nevis, K.R., Jahangiri, L., Obregon, P., Kikuchi, K., Poss, K.D., Burns, C.E., and Burns, C.G. (2013). Zebrafish second heart field development relies on progenitor specification in anterior lateral plate mesoderm and nkx2.5 function. Development *140*, 1353–1363.

Hami, D., Grimes, A.C., Tsai, H.-J., and Kirby, M.L. (2011). Zebrafish cardiac development requires a conserved secondary heart field. Development *138*, 2389–2398.

Harel, I., Nathan, E., Tirosh-Finkel, L., Zigdon, H., Guimarães-Camboa, N., Evans, S.M., and Tzahor, E. (2009). Distinct origins and genetic programs of head muscle satellite cells. Dev. Cell *16*, 822–832.

Harmon, A.W., and Nakano, A. (2013). Nkx2-5 lineage tracing visualizes the distribution of second heart field-derived aortic smooth muscle. Genesis *51*, 862–869.

Helde, K.A., and Grunwald, D.J. (1993). The DVR-1 (Vg1) transcript of zebrafish is maternally supplied and distributed throughout the embryo. Dev. Biol. *159*, 418–426.

Jao, L.-E., Wente, S.R., and Chen, W. (2013). Efficient multiplex biallelic zebrafish genome editing using a CRISPR nuclease system. Proc. Natl. Acad. Sci. USA *110*, 13904–13909.

Jerome, L.A., and Papaioannou, V.E. (2001). DiGeorge syndrome phenotype in mice mutant for the T-box gene, Tbx1. Nat. Genet. *27*, 286–291.

Jin, S.C., Homsy, J., Zaidi, S., Lu, Q., Morton, S., DePalma, S.R., Zeng, X., Qi, H., Chang, W., Sierant, M.C., et al. (2017). Contribution of rare inherited and de novo variants in 2,871 congenital heart disease probands. Nat. Genet. *49*, 1593–1601.

Karkera, J.D., Lee, J.S., Roessler, E., Banerjee-Basu, S., Ouspenskaia, M.V., Mez, J., Goldmuntz, E., Bowers, P., Towbin, J., Belmont, J.W., et al. (2007). Loss-of-function mutations in growth differentiation factor-1 (GDF1) are associated with congenital heart defects in humans. Am. J. Hum. Genet. *81*, 987–994.

Kelly, R.G., and Papaioannou, V.E. (2007). Visualization of outflow tract development in the absence of Tbx1 using an FgF10 enhancer trap transgene. Dev. Dyn. *236*, 821–828.

Kelly, R.G., Jerome-Majewska, L.A., and Papaioannou, V.E. (2004). The del22q11.2 candidate gene Tbx1 regulates branchiomeric myogenesis. Hum. Mol. Genet. *13*, 2829–2840.

Kochilas, L., Merscher-Gomez, S., Lu, M.M., Potluri, V., Liao, J., Kucherlapati, R., Morrow, B., and Epstein, J.A. (2002). The role of neural crest during cardiac development in a mouse model of DiGeorge syndrome. Dev. Biol. *251*, 157–166.

Kong, P., Racedo, S.E., Macchiarulo, S., Hu, Z., Carpenter, C., Guo, T., Wang, T., Zheng, D., and Morrow, B.E. (2014). Tbx1 is required autonomously for cell survival and fate in the pharyngeal core mesoderm to form the muscles of mastication. Hum. Mol. Genet. *23*, 4215–4231.

Lee, K.H., Xu, Q., and Breitbart, R.E. (1996). A new tinman-related gene, nkx2.7, anticipates the expression of nkx2.5 and nkx2.3 in zebrafish heart and pharyngeal endoderm. Dev. Biol. *180*, 722–731.

Lee, E.C., Yu, D., Martinez de Velasco, J., Tessarollo, L., Swing, D.A., Court, D.L., Jenkins, N.A., and Copeland, N.G. (2001). A highly efficient Escherichia coli-based chromosome engineering system adapted for recombinogenic targeting and subcloning of BAC DNA. Genomics *73*, 56–65.

Lewin, M.B., Lindsay, E.A., Jurecic, V., Goytia, V., Towbin, J.A., and Baldini, A. (1997). A genetic etiology for interruption of the aortic arch type B. Am. J. Cardiol. *80*, 493–497.

Liao, J., Kochilas, L., Nowotschin, S., Arnold, J.S., Aggarwal, V.S., Epstein, J.A., Brown, M.C., Adams, J., and Morrow, B.E. (2004). Full spectrum of malformations in velo-cardio-facial syndrome/DiGeorge syndrome mouse models by altering Tbx1 dosage. Hum. Mol. Genet. *13*, 1577–1585.

Lindsay, E.A., and Baldini, A. (2001). Recovery from arterial growth delay reduces penetrance of cardiovascular defects in mice deleted for the DiGeorge syndrome region. Hum. Mol. Genet. *10*, 997–1002.

Lindsay, E.A., Botta, A., Jurecic, V., Carattini-Rivera, S., Cheah, Y.C., Rosenblatt, H.M., Bradley, A., and Baldini, A. (1999). Congenital heart disease in mice deficient for the DiGeorge syndrome region. Nature *401*, 379–383.

Lyons, M.S., Bell, B., Stainier, D., and Peters, K.G. (1998). Isolation of the zebrafish homologues for the tie-1 and tie-2 endothelium-specific receptor tyrosine kinases. Dev. Dyn. *212*, 133–140.

McCurley, A.T., and Callard, G.V. (2008). Characterization of housekeeping genes in zebrafish: male-female differences and effects of tissue type, developmental stage and chemical treatment. BMC Mol. Biol. *9*, 102.

McDonald-McGinn, D.M., Driscoll, D.A., Emanuel, B.S., Goldmuntz, E., Clark, B.J., 3rd, Solot, C., Cohen, M., Schultz, P., LaRossa, D., Randall, P., and Zackai, E.H. (1997). Detection of a 22q11.2 deletion in cardiac patients suggests a risk for velopharyngeal incompetence. Pediatrics *99*, E9.

McDonald-McGinn, D.M., Sullivan, K.E., Marino, B., Philip, N., Swillen, A., Vorstman, J.A.S., Zackai, E.H., Emanuel, B.S., Vermeesch, J.R., Morrow, B.E., et al. (2015). 22q11.2 deletion syndrome. Nat. Rev. Dis. Primers *1*, 15071.

Merscher, S., Funke, B., Epstein, J.A., Heyer, J., Puech, A., Lu, M.M., Xavier, R.J., Demay, M.B., Russell, R.G., Factor, S., et al. (2001). TBX1 is responsible for cardiovascular defects in velo-cardio-facial/DiGeorge syndrome. Cell *104*, 619–629.

Montague, T.G., and Schier, A.F. (2017). Vg1-Nodal heterodimers are the endogenous inducers of mesendoderm. Elife *6*, e28183.

Nevis, K., Obregon, P., Walsh, C., Guner-Ataman, B., Burns, C.G., and Burns, C.E. (2013). Tbx1 is required for second heart field proliferation in zebrafish. Dev. Dyn. *242*, 550–559.

Novikov, N., and Evans, T. (2013). Tmem88a mediates GATA-dependent specification of cardiomyocyte progenitors by restricting WNT signaling. Development *140*, 3787–3798.

Paffett-Lugassy, N., Singh, R., Nevis, K.R., Guner-Ataman, B., O'Loughlin, E., Jahangiri, L., Harvey, R.P., Burns, C.G., and Burns, C.E. (2013). Heart field origin of great vessel precursors relies on nkx2.5-mediated vasculogenesis. Nat. Cell Biol. *15*, 1362–1369.

Paffett-Lugassy, N., Novikov, N., Jeffrey, S., Abrial, M., Guner-Ataman, B., Sakthivel, S., Burns, C.E., and Burns, C.G. (2017). Unique developmental trajectories and genetic regulation of ventricular and outflow tract progenitors in the zebrafish second heart field. Development *144*, 4616–4624.

Pelliccia, J.L., Jindal, G.A., and Burdine, R.D. (2017). Gdf3 is required for robust Nodal signaling during germ layer formation and left-right patterning. Elife *6*, e28635.

Peterson, A.G., Wang, X., and Yost, H.J. (2013). Dvr1 transfers left-right asymmetric signals from Kupffer's vesicle to lateral plate mesoderm in zebrafish. Dev. Biol. *382*, 198–208.

Piotrowski, T., and Nüsslein-Volhard, C. (2000). The endoderm plays an important role in patterning the segmented pharyngeal region in zebrafish (Danio rerio). Dev. Biol. *225*, 339–356.

Piotrowski, T., Schilling, T.F., Brand, M., Jiang, Y.J., Heisenberg, C.P., Beuchle, D., Grandel, H., van Eeden, F.J., Furutani-Seiki, M., Granato, M., et al. (1996). Jaw and branchial arch mutants in zebrafish II: anterior arches and cartilage differentiation. Development *123*, 345–356.

Piotrowski, T., Ahn, D.-G., Schilling, T.F., Nair, S., Ruvinsky, I., Geisler, R., Rauch, G.-J., Haffter, P., Zon, L.I., Zhou, Y., et al. (2003). The zebrafish van gogh mutation disrupts tbx1, which is involved in the DiGeorge deletion syndrome in humans. Development *130*, 5043–5052.

Rauch, A., Hofbeck, M., Leipold, G., Klinge, J., Trautmann, U., Kirsch, M., Singer, H., and Pfeiffer, R.A. (1998). Incidence and significance of 22q11.2 hemizygosity in patients with interrupted aortic arch. Am. J. Med. Genet. *78*, 322–331.

Ryan, A.K., Goodship, J.A., Wilson, D.I., Philip, N., Levy, A., Seidel, H., Schuffenhauer, S., Oechsler, H., Belohradsky, B., Prieur, M., et al. (1997). Spectrum

of clinical features associated with interstitial chromosome 22q11 deletions: a European collaborative study. J. Med. Genet. *34*, 798–804.

Scambler, P.J. (2000). The 22q11 deletion syndromes. Hum. Mol. Genet. *9*, 2421–2426.

Scambler, P.J. (2010). 22q11 deletion syndrome: a role for TBX1 in pharyngeal and cardiovascular development. Pediatr. Cardiol. *31*, 378–390.

Schilling, T.F., and Kimmel, C.B. (1994). Segment and cell type lineage restrictions during pharyngeal arch development in the zebrafish embryo. Development *120*, 483–494.

Schilling, T.F., and Kimmel, C.B. (1997). Musculoskeletal patterning in the pharyngeal segments of the zebrafish embryo. Development *124*, 2945–2960.

Schilling, T.F., Piotrowski, T., Grandel, H., Brand, M., Heisenberg, C.P., Jiang, Y.J., Beuchle, D., Hammerschmidt, M., Kane, D.A., Mullins, M.C., et al. (1996). Jaw and branchial arch mutants in zebrafish I: branchial arches. Development *123*, 329–344.

Schoenebeck, J.J., Keegan, B.R., and Yelon, D. (2007). Vessel and blood specification override cardiac potential in anterior mesoderm. Dev. Cell *13*, 254–267.

Schulte-Merker, S., van Eeden, F.J., Halpern, M.E., Kimmel, C.B., and Nüsslein-Volhard, C. (1994). no tail (ntl) is the zebrafish homologue of the mouse T (Brachyury) gene. Development *120*, 1009–1015.

Serbedzija, G.N., Chen, J.N., and Fishman, M.C. (1998). Regulation in the heart field of zebrafish. Development *125*, 1095–1101.

Stanley, E.G., Biben, C., Elefanty, A., Barnett, L., Koentgen, F., Robb, L., and Harvey, R.P. (2002). Efficient Cre-mediated deletion in cardiac progenitor cells conferred by a 3′UTR-ires-Cre allele of the homeobox gene Nkx2-5. Int. J. Dev. Biol. *46*, 431–439.

Suster, M.L., Abe, G., Schouw, A., and Kawakami, K. (2011). Transposon-mediated BAC transgenesis in zebrafish. Nat. Protoc. *6*, 1998–2021.

Thomsen, G.H., and Melton, D.A. (1993). Processed Vg1 proteins is an axial mesoderm inducer in Xenopus. Cell *74*, 433–441.

Trapnell, C., Pachter, L., and Salzberg, S.L. (2009). TopHat: discovering splice junctions with RNA-Seq. Bioinformatics *25*, 1105–1111.

Trapnell, C., Roberts, A., Goff, L., Pertea, G., Kim, D., Kelley, D.R., Pimentel, H., Salzberg, S.L., Rinn, J.L., and Pachter, L. (2012). Differential gene and transcript expression analysis of RNA-seq experiments with TopHat and Cufflinks. Nat. Protoc. *7*, 562–578.

Vitelli, F., Morishima, M., Taddei, I., Lindsay, E.A., and Baldini, A. (2002). Tbx1 mutation causes multiple cardiovascular defects and disrupts neural crest and cranial nerve migratory pathways. Hum. Mol. Genet. *11*, 915–922.

Wang, W., Razy-Krajka, F., Siu, E., Ketcham, A., and Christiaen, L. (2013). NK4 antagonizes Tbx1/10 to promote cardiac versus pharyngeal muscle fate in the ascidian second heart field. PLoS Biol. *11*, e1001725.

Xu, H., Morishima, M., Wylie, J.N., Schwartz, R.J., Bruneau, B.G., Lindsay, E.A., and Baldini, A. (2004). Tbx1 has a dual role in the morphogenesis of the cardiac outflow tract. Development *131*, 3217–3227.

Xu, H., Cerrato, F., and Baldini, A. (2005). Timed mutation and cell-fate mapping reveal reiterated roles of Tbx1 during embryogenesis, and a crucial function during segmentation of the pharyngeal system via regulation of endoderm expansion. Development *132*, 4387–4395.

Yagi, H., Furutani, Y., Hamada, H., Sasaki, T., Asakawa, S., Minoshima, S., Ichida, F., Joo, K., Kimura, M., Imamura, S., et al. (2003). Role of TBX1 in human del22q11.2 syndrome. Lancet *362*, 1366–1373.

Yu, D., Ellis, H.M., Lee, E.C., Jenkins, N.A., Copeland, N.G., and Court, D.L. (2000). An efficient recombination system for chromosome engineering in Escherichia coli. Proc. Natl. Acad. Sci. USA *97*, 5978–5983.

Zhang, Z., Cerrato, F., Xu, H., Vitelli, F., Morishima, M., Vincentz, J., Furuta, Y., Ma, L., Martin, J.F., Baldini, A., and Lindsay, E. (2005). Tbx1 expression in pharyngeal epithelia is necessary for pharyngeal arch artery development. Development *132*, 5307–5315.

Zhang, Z., Huynh, T., and Baldini, A. (2006). Mesodermal expression of Tbx1 is necessary and sufficient for pharyngeal arch and cardiac outflow tract development. Development *133*, 3587–3595.

Zhou, Y., Cashman, T.J., Nevis, K.R., Obregon, P., Carney, S.A., Liu, Y., Gu, A., Mosimann, C., Sondalle, S., Peterson, R.E., et al. (2011). Latent TGF-β binding protein 3 identifies a second heart field in zebrafish. Nature *474*, 645–648.

## STAR★METHODS

### KEY RESOURCES TABLE

| REAGENT or RESOURCE | SOURCE | IDENTIFIER |
|---|---|---|
| Antibodies | | |
| Mouse monoclonal MF20 | Deposited to the Developmental Studies Hybridoma Bank by Fischman, D.A. | DSHB Hybridoma Product MF20 |
| Rabbit polyclonal anti-Elastin-2 | Gift from Fred Keeley | N/A |
| Rabbit polyclonal anti-GFP | Invitrogen | Cat# A11122; RRID:AB_221569 |
| Mouse monoclonal anti-GFP | Santa Cruz Biotechnology | Cat#sc-9996; RRID:AB_627695 |
| Goat anti-Mouse IgG (H+L) Cross-Absorbed Secondary Antibody, Alexa Fluor 555 | Thermo Fisher Scientific | Cat# A-21422; RRID:AB_2535844 |
| Goat anti-Rabbit IgG (H+L) Cross-Absorbed Secondary Antibody, Alexa Fluor 488 | Thermo Fisher Scientific | Cat# A-11008; RRID:AB_143165 |
| Goat anti-Mouse IgG2a (H+L) Cross-Absorbed Secondary Antibody, Alexa Fluor 488 | Thermo Fisher Scientific | Cat# A-21131; RRID:AB_2535771 |
| Goat anti-Rabbit IgG (H+L) Cross-Adsorbed Secondary Antibody, Alexa Fluor 555 | Thermo Fisher Scientific | Cat# A-21428; RRID:AB_2535849 |
| Chemicals, Peptides, and Recombinant Proteins | | |
| Ethyl-Aminobenzoate methanesulfonate, MS222 | Sigma-Aldrich | Cat#E10521 |
| Nitro-Blue Tetrazolium Chloride | Promega | Cat#S380C |
| 5-Bromo-4-Chloro-3-Indolyphosposphate p-Toluidine | Promega | Cat#S381C |
| Trizol | Invitrogen | Cat#15596-026 |
| Phenol:Chloroform:Isoamyl Alcohol | Sigma-Aldrich | Cat#P3803 |
| SB505124 | Sigma-Aldrich | Cat#S2186 |
| Critical Commercial Assays | | |
| DIG RNA Labeling Kit (SP6/T7) | Roche | Cat#11175025910 |
| Click-iT Plus TUNEL Assay for *In Situ* Apoptosis Detection, Alexa Fluor 647 dye | Thermo Fisher Scientific | Cat#C10619 |
| SV Total RNA Isolation System | Promega | Cat#Z3100 |
| TruSeq RNA Library Prep Kit v2, Set B | Illumina | RS-122-2002 |
| SuperScript III First-Strand Synthesis System | Thermo Fisher Scientific | Cat#18080051 |
| Power SYBER Green PCR Master Mix | Thermo Fisher Scientific | Cat#4367659 |
| pCRBluntII TOPO Cloning Kit | Invitrogen | Cat#K280002 |
| RNAScope Multiplex Fluorescent Reagent Kit | ACD | Cat#320850 |
| Deposited Data | | |
| RNA Sequencing Data | This paper | GEO: GSE103120 |
| Experimental Models: Organisms/Strains | | |
| Zebrafish: *van gogh*$^{tu285}$ | Piotrowski et al., 1996<br>Schilling et al., 1996 | ZFIN: ZDB-GENO-030805-5 |
| Zebrafish: *kdrl:GFP*$^{la116}$ | Choi et al., 2007 | ZFIN: ZDB-ALT-070529-1 |
| Zebrafish: *nkx2.5:ZsYellow*$^{fb7}$ | Zhou et al., 2011 | ZFIN: ZDB-ALT-111115-8 |
| Zebrafish: *tbx1:GFP*$^{fb25}$ | This paper | N/A |
| Zebrafish: *nkx2.5:Kaede*$^{fb9}$ | Guner-Ataman et al., 2013 | ZFIN ID: ZDB-GENO-130411-2 |
| Zebrafish: *tbx1:mKate2P2Acre*$^{fb23}$, *Tg(tbx1:cre)* | This paper | N/A |
| Zebrafish: *3.5ubb:loxP-lacZ-loxP-eGFP*$^{cn2}$ *Tg(ubi:HULK)* | Di Donato., 2016 | N/A |
| Zebrafish: *kdrl:loxP-AmCyan-loxP-ZsYellow*$^{fb3}$ *Tg(kdrl:CSY)* | Zhou et al., 2011 | ZFIN ID: ZDB-GENO-111115-4 |

(*Continued on next page*)

*Continued*

| REAGENT or RESOURCE | SOURCE | IDENTIFIER |
|---|---|---|
| Oligonucleotides | | |
| Primers for *vgo/tbx1* genotyping: | Nevis et al., 2013 | N/A |
| Forward: 5′-CCAGCACGCCTACAACTATT-3′ | | |
| Reverse: 5′-AGCAAGGAGCCCTTTAGCAC-3′ | | |
| Primers for *gdf3* qPCR: | This paper | N/A |
| Forward: 5′-GTTTCCTCCAGGATTGGGCC-3′ | | |
| Reverse: 5′-GGCCCAATCCTGGAGGAAAC-3′ | | |
| Primers for *nkx2.5* qPCR: | This paper | N/A |
| Forward: 5′-CAGTGCTTCAGGCTTTTACG-3′ | | |
| Reverse: 5′-ATCCAGCTTCAGATCTTCACC-3′ | | |
| Primers for *tbx1* qPCR: | This paper | N/A |
| Forward: 5′-CCGTCACAGCCTATCAAAACC-3′ | | |
| Reverse: 5′-GTTCGAGCAAAAGCACTCATG-3′ | | |
| Primers for *18S rRNA* qPCR: | McCurley and Callard, 2008 | N/A |
| Forward: 5′-TCGCTAGTTGGCATCGTTTATG-3′ | | |
| Reverse: 5′-CGGAGGTTCGAAGACGATCA-3′ | | |
| Primers for generating *gdf3* mutant: | This paper | N/A |
| Forward: 5′-GTTTCCTCCAGGATTGGGCC-3′ | | |
| Reverse: 5′-GGCCCAATCCTGGAGGAAAC-3′ | | |
| Primers to test *gdf3* mutation rate: | This paper | N/A |
| Forward: 5′-AGCAACTCTCGTTGGCGCAG-3′ | | |
| Reverse: 5′-GGGAACGCAACAGGGCTGAG-3′ | | |
| Primers for *gdf3* fragment analysis: | This paper | N/A |
| Forward: 5′-ACCACACTGAAGGGAGTAACG-3′ | | |
| Reverse: 5′-6-Fam-CAATCCTGCCAGCCTACATCT-3′ | | |
| Recombinant DNA | | |
| pBSK-*tie1* | Lyons et al., 1998 | N/A |
| pBSK-*nkx2.5* | Novikov and Evans, 2013 | N/A |
| Tbx1 BAC | Gift from Bruce Barut and Leonard I. Zon | DKEY-115P14 |
| pBSK-*hand2* | Schoenebeck et al., 2007 | N/A |
| pExpress1-*tbx1* | Nevis et al., 2013 | N/A |
| MDR1734-202794042 (Danio rerio *gdf3*) | GE Dharmacon | Cat# MDR1734-202794042 |
| pBSK-*no tail* | Schulte-Merker et al., 1994 | N/A |
| pSP64TBVg1 vector (Vg1/Gdf3 mRNA) | Thomsen and Melton, 1993 | Addgene Cat#15071 |
| pCS2-nls-zCas9-nls | Jao et al., 2013 | Addgene #47929 |
| Software and Algorithms | | |
| NIS-Elements | Nikon Instruments | N/A |
| Fiji/ImageJ | NIH | RRID:SCR_002285 |
| GraphPad Prism 7 | GraphPad Software | N/A |
| Spotfire | TIBCO | N/A |
| Other | | |
| 4′,6-diamidino-2-phenylindole dihydrochloride | Invitrogen | Cat#D1306 |
| RNAscope probe Dr- tbx1 | ACD | Cat#429581 |
| RNAscope probe Dr-nkx2.5-C2 | ACD | Cat#429591-C2 |
| RNAscope probe Dr-dvr1-C3 | ACD | Cat#429601-C3 |

## CONTACT FOR REAGENT AND RESOURCE SHARING

Further information and requests for resources and reagents should be directed to and will be fulfilled by the Lead Contact, Caroline E. Burns (cburns6@mgh.harvard.edu).

## EXPERIMENTAL MODEL AND SUBJECT DETAILS

Zebrafish were bred, grown, and maintained according to the protocols approved by the Institutional Animal Care and Use Committees of Massachusetts General Hospital. Experimental and control animals of the same age, weight, and underlying health (apart from differences caused by the mutations under study) were analyzed. As zebrafish are sexually indistinguishable visually and genetically during early development, sex is not considered to be a relevant biological variable in embryonic studies. The following strains were used: *van gogh*$^{tu285}$(Piotrowski et al., 1996; Schilling et al., 1996); *Tg(kdrl:GFP)*$^{la116}$(Choi et al., 2007), *Tg(nkx2.5:ZsYellow)*$^{fb7}$(Zhou et al., 2011), *Tg(nkx2.5:Kaede)*$^{fb9}$(Guner-Ataman et al., 2013); *Tg(kdrl:loxP-AmCyan-loxP-ZsYellow)*$^{fb\ 3}$ [referred to here as *Tg(kdrl:CSY)]* (Zhou et al., 2011); *Tg(3.5ubb:loxP-lacZ-loxP*-eGFP)$^{cn2}$ [referred to here as *Tg(ubi:HULK)]*(Di Donato et al., 2016); *Tg(tbx1:mKate2P2Acre)*$^{fb23}$ and *Tg(tbx1:GFP)*$^{fb25}$ (see below). Live embryos were kept at 28.5°C and anesthetized in standard embryo media containing 0.4% tricaine (ethyl 3-aminobenzoate methanesulfonate, MS222; Sigma-Aldrich).

## METHOD DETAILS

### Zebrafish Whole Mount Immunohistochemistry

Embryos were fixed at 4°C overnight in 4% paraformaldehyde (PFA) and rinsed the following day in PBSTw (0.1% Tween-20 in PBS). Embryos were processed for immunohistochemistry as previously described (Abrial et al., 2017). Primary antibodies recognize GFP (B-2 mouse monoclonal, Santa Cruz Biotechnology; 1:50 and rabbit polyclonal, Invitrogen; 1:200), MF20 (mouse monoclonal, Developmental Hybridoma Bank, University of Iowa; 1:50) and Elastin-2 (gift from Fred Keeley; 1:1,000). Secondary antibodies, Alexa Fluor 555 goat anti-mouse IgG, Alexa Fluor 555 goat anti-rabbit IgG, Alexa Fluor 488 goat anti-mouse IgG2a and Alexa Fluor 488 goat anti-rabbit (Thermo Fisher Scientific) were all used at 1:400 dilutions.

### Zebrafish Whole Mount *In Situ* Hybridization

600 base pairs between the 10th and 609th nucleotides of the zebrafish *gdf3* coding sequence (amplified from clone MDR1734-202794042, GE Dharmacon) were cloned into pCRBluntII TOPO vector (Invitrogen) to generate *gdf3* riboprobes. Single whole mount *in situ* hybridizations were performed as previously described (Guner-Ataman et al., 2013) using digoxygenin-labeled antisense RNA riboprobes to *tie1* (Lyons et al., 1998), *hand2* (Schoenebeck et al., 2007), *gdf3* (see above), and *no tail* (*ntl*) (Schulte-Merker et al., 1994). Probes were synthesized using a DIG RNA Labeling Kit (Roche). Specifically, riboprobes to *tie1* was generated by linearization with SpeI and *in vitro* transcribed with T7 polymerase (Paffett-Lugassy et al., 2013), riboprobes to *nkx2.5* and *tbx1* were generated by linearization with EcoRI and *in vitro* transcribed with T7 polymerase (Nevis et al., 2013), riboprobes to *hand2* were generated by linearization with NotI and *in vitro* transcribed with T7 polymerase, while those to *gdf3* were generated by linearization with XhoI and *in vitro* transcribed with SP6 polymerase. The *ntl* plasmid was linearized with XhoI and *in vitro* transcribed with T7. Nitro-Blue Tetrazolium Chloride/5-Bromo-4-Chloro-3′-Indolyphosphate p-Toluidine (NBT/BCIP; Promega) chromogenic substrates were used for the colormetric reaction. Processed embryos were mounted on glass slides in 100% glycerol and imaged at four focal planes on a Nikon 80i compound microscope (Nikon Instruments Inc.) with a mounted Retiga 2000R high speed CCD camera (QImaging) or an Excelis AU600HDS HD Camera (Accu-Scope). The individual focal plane images were merged into a single image with Zerene Stacker Software (Build T201412212230).

### RNAscope Whole Mount *In Situ* Hybridization

6 somite stage embryos were fixed for 4 hr in 4% PFA, washed with PBSTw (PBS with 0.1% Tween), and dehydrated in methanol at −20°C overnight. Whole mount fluorescent *in situ* hybridization was performed utilizing RNAscope Multiplex Fluorescent Reagent Kit (Advanced Cell Diagnostics) as previously described (Gross-Thebing et al., 2014). RNAscope riboprobes to *nkx2.5, tbx1 and gdf3* were hybridized overnight at 40°C at a 50:1:1 ratio, respectively. Following the final labeling reaction, embryos were incubated with DAPI solution overnight at 4°C to visualize nuclei. The embryos were analyzed using 405nm, 488nm, 561nm, 641nm lasers on Nikon A1SiR Confocal Microscope (Nikon Instruments Inc.).

### Kaede Photoconversion

Wild-type and *tbx1* mutant embryos carrying the *nkx2.5:Kaede* transgene were photoconverted using a Nikon A1SiR Confocal Microscope (Nikon Instruments Inc.) and a 20X objective. 16 somite stage embryos were mounted in 0.9% low melting point agarose (Sigma-Aldrich) on 35 mm MatTek glass bottom Petri dishes (MatTek Corporation). Prior to photoconversion, embryos were imaged using a 488 laser to detect green fluorescence. Embryos were then exposed continually to UV light using the 405 mm laser for 3 min. Photoconverted animals were kept in a 28°C incubator until 32 hr post fertilization, anesthetized with 0.04% tricaine (Sigma-Aldrich), and imaged by confocal microscopy. The resulting z stack images were analyzed using FiJi/ImageJ software.

### Generation of The Tg(tbx1:mKate2P2Acre) and Tg(tbx1:GFP) Lines

λ-red-mediated BAC recombineering (Lee et al., 2001; Yu et al., 2000) was used to replace the coding sequence in the first exon of the *tbx1* locus in BAC DKEY-115P14 with *mKate2P2Acre* or *GFP* and to flank the BAC insert with ATI and ITK cassettes (Zhou et al., 2011) to generate the *tbx1:mKate2P2Acre* and *tbx1:GFP* transgenic lines respectively. DKEY-115P14 contains approximately 67 Kb and 83 Kb of genomic sequence upstream and downstream of the first *tbx1* exon, respectively. For germline transmission, the BAC was co-injected with Tol2 transposase mRNA (Suster et al., 2011) into the cell of one-cell stage embryos. Candidate founders were selected based on fluorescence, grown to adulthood, and screened for germline transmission in test crosses.

### TUNEL Staining

*Tg(tbx1:GFP)* embryos were fixed at the 6 somite stage in 4% paraformaldehyde in PBS. Apoptosis was detected by TUNEL labeling using the Alexa 647 *in situ* cell death detection kit (Roche). The embryos were immunostained with GFP antibodies (B-2 mouse monoclonal, Santa Cruz Biotechnology; 1:200). Alexa Fluor 488 goat anti-mouse IgG2a (Thermo Fisher Scientific) was used as a secondary antibody. Nuclei were counterstained with DAPI. The embryos were analyzed using a Nikon A1SiR Confocal Microscope (Nikon Instruments Inc.). The number of apoptotic cells throughout the embryos and in the presumptive *nkx2.5*-positive areas (defined as a region of 120 μm x 140 μm on both sides of the embryo) were measured using ImageJ software.

### Zebrafish Lineage Tracing

*Tg(tbx1:mKate2P2Acre);Tg(ubi:HULK)* double transgenic embryos were analyzed for GFP reporter signal using Nikon A1SiR Confocal Microscope (Nikon Instruments). Specifically, double transgenic animals were fixed overnight at 3 days post fertilization (dpf) with 4% PFA and processed by double immunohistochemistry for GFP and MF20. Similarly, *Tg(tbx1:mKate2P2Acre); Tg(kdrl:CSY)* double transgenic embryos were analyzed live for ZsYellow reporter fluorescence by confocal imaging using 405 nm blue diode and 514nm Argon lasers on a Zeiss LSM5 Pascal Laser Scanning Microscope (Carl Zeiss MicroImaging).

### RNA-Sequencing and Library Preparation

At the 6 somite stage, the tip of the tail was dissected using iridectomy scissors for genotyping while the remainder of the embryo placed in Trizol Reagent (Invitrogen).

Total RNA was extracted from *tbx1* null and wild-type embryos using SV Total RNA Isolation System (Promega). RNA integrity and concentration were assessed on a Fragment Analyzer (Advanced Analytical). The mRNA was purified by polyA-tail enrichment, fragmented, and reverse transcribed into cDNA (Illumina TruSeq). The resulting cDNA samples were then end-repaired and adaptor-ligated using the SPRIworks Fragment Library System I (Beckman Coulter Genomics) and indexed during amplification. Libraries were quantified using the Fragment Analyzer (Advanced Analytical) and qPCR before being loaded for paired-end sequencing 2X40 nucleotide using the Illumina HiSeq 2000.

### RNA-Seq Data Processing

Reads were aligned against the Zebrafish danRer7/ZV9 genome using tophat v. 2.0.8 (tophat -p 8–no-novel-juncs–segment-length 20–solexa1.3-quals–read-realign-edit-dist 0–library-type fr-unstranded -G Danio_rerio.Zv9.70.chr.gtf danRer7) (Trapnell et al., 2009). Gene expression was estimated using cufflinks v. 2.1.1 (cufflinks -p 8 -u -b danRer7.fa–compatible-hits-norm–library-type fr-unstranded -G Danio_rerio.Zv9.70.chr.gtf) (Trapnell et al., 2012). The resulting output files were merged and compared using cuffmerge (cuffmerge -p 8 -s danRer7.fa -g Danio_rerio.Zv9.70.chr.gtf) and differential expression was performed using cuffdiff v. 2.1.1 (cuffdiff -p 8 -u–library-norm-method geometric–dispersion-method per-condition–min-reps-for-js-test 2 -b danRer7.fa–compatible-hits-norm merged_gtf/merged.gtf). The volcano plot was generated using the cuffdiff output with Spotfire (Tibco).

RNA from wild-type and *tbx1* mutant embryos were extracted using Trizol reagent (Invitrogen) and phenol:chloroform (Sigma-Aldrich). RNA was transcribed to cDNA using the SuperScript III First-Strand Synthesis System (Thermo Fisher Scientific). Quantitative PCR was performed using Power SYBER Green PCR Master Mix (Thermo Fisher Scientific) and primers for *nkx2.5* [(Nkx2.5F (5′- CAGTGCTTCAGGCTTTTACG-3′), Nkx2.5R (5′-ATCCAGCTTCAGATCTTCACC-3′)], *gdf3* [Gdf3F(5′-CACACTGGATTGGGTTT CATTC-3′), Gdf3R (5′ TCTGCATGTCTATGGCGTAAG-3′)], *tbx1* [Tbx1F (CCGTCACAGCCTATCAAAACC), Tbx1R (GTTCGAG CAAAAGCACTCATG)] and β-*actin* [β-ActinF (5′-ATCTTCACTCCCCTTGTTCAC-3′), β-ActinR (5′TCATCTCCAGCAAAACCGG-3′)] (Zhou et al., 2011). Threshold cycles (Cts) for these select transcripts were normalized to 18S ribosomal RNA (McCurley and Callard, 2008) prior to calculating fold differences in gene expression between experimental groups.

### *gdf3* (*vg1*) mRNA Synthesis

pSP64TBVg1 vector (Addgene # 15071) was linearized with EcoRI and transcribed with SP6 to generate *gdf3* mRNA. 5 pg RNA was injected into one-cell staged wild-type and *tbx1* mutant embryos. Embryos were fixed with 4% paraformaldehyde at 50% epiboly and 6 somite stage for processing by *in situ* hybridization with *ntl* and *nkx2.5* riboprobes, respectively.

### Generation of a *gdf3* Null Allele by CRISPR-Cas9 Genome Editing

Potential CRISPR target sites were identified by manually scanning the *gdf3* sequence between the region encoding the propeptide and homodimer domains for a $GGN_{19}GG$ sequence. Forward 5′-GTTTCCTCCAGGATTGGGCC-3′ and reverse 5′-GGC

CCAATCCTGGAGGAAAC-3′ primers targeting the cut site were annealed as previously described (Jao et al., 2013). pCS2-nls-zCas9-nls (Addgene #47929) was linearized and *in vitro* transcribed to obtain Cas9 mRNA as previously described (Jao et al., 2013). gRNA and Cas9 RNA were purified using phenol/chloroform and injected at 50 ng/μl concentrations into the cell of 1-cell-stage embryos. The mutation rate was determined by next-generation sequencing of the PCR fragment amplified using forward 5′-AGCA ACTCTCGTTGGCGCAG-3′ and reverse 5′- GGGAACGCAACAGGGCTGAG −3′ primers.

### Gdf3 Mutant Genotyping

The *gdf3*$^{fb20}$ allele has a 10 base pair (bp) deletion at exon 2 (Figure 5L). Forward 5′-ACCACACTGAAGGGAGTAACG-3′ and 6-Fam attached fluorescent reverse 5′-CAATCCTGCCAGCCTACATCT-3′ primers were used to amplify a fragment of *gdf3* allele. Microsatellite fragment analysis was performed following PCR amplification.

Heterozygous embryos had fragments detected at 369 (wild-type) and 359 bp (mutant), whereas homozygous mutant embryos only had the 359 bp fragment.

### Small Molecule Treatment

SB-505124 compound (Sigma-Aldrich) was dissolved in DMSO at a final concentration of 10 mM. Embryos were incubated in embryo medium containing SB-505124 at the indicated doses (20, 40, and 80μM) starting from 75% epiboly (Figures 6 and 7). A subset of chemically treated embryos were fixed with 4% PFA at 6 somite stage to evaluate *nkx2.5* and/or *tbx1* expression and at 38 hr post fertilization (hpf) to analyze *tie1* transcripts by *in situ* hybridization. Another set of treated embryos were fixed with 4% PFA at 3 days post fertilization and immunostained to assess HM and OFT development with antibodies against MF20 and Elastin-2. Embryos were treated with 10μM SB-505124 and DMSO starting from 4 hpf (Figure S7). The gross morphology was analyzed at 28 hpf.

## QUANTIFICATION AND STATISTICAL ANALYSIS

Sample sizes, statistical tests, and p values are indicated in each figure legend. Embryos were genotyped for *tbx1* mutant alleles subsequent to live imaging, immunohistochemistry, *in situ* hybridization, TUNEL labeling, or Kaede fate-mapping. Differences in the distribution of apoptotic cells between the anterior lateral plate of the control and *tbx1* mutants was expressed as mean ± SD, and an unpaired two-tailed t test was performed using GraphPad Prism software. The p value for the RNA-seq data ($p < 0.05$) was calculated using cuffdiff v2.1.1 algorithms (Trapnell et al., 2012). Differential expression of *gdf3*, *nkx2.5* and *tbx1* between the control and the *tbx1* mutants were evaluated by qPCR. Statistical analysis for the qPCR data was performed with GraphPad Prism software using unpaired two-tailed t test. The average number of pharyngeal clusters per control and treated groups were calculated and categorized into 2 classes. Similarly, the HMs and OFT of the control and treated embryos were categorized according to their phenotypes into 2 classes. Percentage of embryos per class is demonstrated using GraphPad Prism software. To quantify *tbx1* and *nkx2.5* expression in embryos processed by whole mount *in situ* hybridization, masks encompassing the entire embryo or the *in situ* hybridization signal (purple) were generated manually in Adobe Photoshop. The area of each mask was measured using ImageJ software. For each embryo, signal area was normalized to that of the whole embryo and expressed as a percentage and the results were expressed as mean ± SD. Mask creation and area measurements were performed blinded to embryo genotype. Differences between the treatment groups for were assessed by one-way ANOVA followed by Tukey's multiple comparisons test. The qPCR experiment was performed in biological triplicates with all other experiments performed in biological duplicates.

## DATA AND SOFTWARE AVAILABILITY

The RNA-seq data that support the findings in Figures 5 and S4 are available under accession number GEO: GSE103120 at the Gene Expression Omnibus.